Thesis for the Degree of Doctor of Philosophy

Noninvasive Bi-graphical Analysis for Parametric Imaging of Slowly Reversible Neuroreceptor Binding with Dynamic Brain PET

지연가역 신경수용체 결합 파라메트릭 영상화를 위한 동적 뇌 PET 기반 비침습적 이중도표분석법

February 2016

Department of Brain and Cognitive Sciences

Graduate School of Natural Sciences

Seoul National University

Seongho Seo

이학박사 학위논문

Noninvasive Bi-graphical Analysis for Parametric Imaging of Slowly Reversible Neuroreceptor Binding with Dynamic Brain PET

지연가역 신경수용체 결합 파라메트릭 영상화를 위한 동적 뇌 PET 기반 비침습적 이중도표분석법

2016 년 2 월

서울대학교 대학원

자연과학대학 뇌인지과학과

서 성 호

지연가역 신경수용체 결합 파라메트릭 영상화를 위한 동적 뇌 PET 기반 비침습적 이중도표분석법

지도 교수 이 재 성

이 논문을 이학박사 학위논문으로 제출함
2015 년 10 월

서울대학교 대학원
뇌인지과학과
서 성 호

서성호의 이학박사 학위논문을 인준함
2015 년 12 월

위 원 장 정 재 민 (인)

부위원장 이 재 성 (인)

위 원 이 종 호 (인)

위 원 김 유 경 (인)

위 원 김 수 진 (인)

Abstract

Noninvasive Linear Method for Parametric Imaging of Neuroreceptor Binding with Dynamic Brain PET

Seongho Seo
Department of Brain and Cognitive Sciences
Graduate School of Natural Sciences
Seoul National University

Tracer kinetic modeling in dynamic positron emission tomography (PET) has been widely used to investigate characteristic distribution pattern or dysfunction of neuroreceptors in brain diseases, by offering a unique tool for generating images of quantitative parameters (or parametric imaging) of neuroreceptor binding. Graphical analysis (GA) is a major technique of parametric imaging, and is based on a simple linear regression model that is linearized and further simplified from a more complex general compartment model.

Although each simple model of various GA methods enables very desirable parametric imaging, it depends on several assumptions that are commonly hard to satisfy simultaneously in parametric imaging for slow kinetic tracers, leading to error in parameter estimates. A combination of two GA methods, a bi-graphical analysis, may improve such intrinsic limitation of GA approaches by taking full advantage of spatiotemporal information captured in dynamic PET data and diverse strengths of individual GA methods.

This thesis focuses on a bi-graphical analysis for parametric imaging of reversible neuroreceptor binding. Firstly, I provide an overview of GA-based parametric image generation with dynamic neuroreceptor PET data. The associated basic concepts in tracer kinetic modeling are presented, including commonly used compartment models and major parameters of interest. Then, technical details of GA approaches for reversible and irreversible radioligands are described considering both arterial-plasma-input-based (*invasive*) and reference-region-input-based (*noninvasive*) models; their underlying assumptions and statistical properties are described in view of parametric imaging.

Next, I present a novel noninvasive bi-graphical analysis for the quantification of a reversible radiotracer binding that may be too slow to reach relative equilibrium (RE) state during PET scans. The proposed method indirectly implements the conventional noninvasive Logan plot, through arithmetic combination of the parameters of two

other noninvasive GA methods and the apparent tissue-to-plasma efflux rate constant for the reference region (k_2'). I investigate its validity and statistical properties, by performing a simulation study with various noise levels and k_2' values, and also evaluate its feasibility for [^{18}F]FP-CIT PET in human brain.

The results reveal that the proposed approach provides a binding-parameter estimation comparable to the Logan plot at low noise levels while improving underestimation caused by non-RE state differently depending on k_2'. Furthermore, the proposed method is able to avoid noise-induced bias of the Logan plot at high noise levels, and the variability of its results is less dependent on k_2' than the Logan plot. In sum, this approach, without issues related to arterial blood sampling if a pre-estimated k_2' is given, could be useful in parametric image generation for slow kinetic tracers staying in a non-RE state within a PET scan.

Keywords: graphical analysis, reference region, parametric image, neuroreceptor imaging, tracer kinetic modeling, dynamic positron emission tomography
Student Number: 2010-30768

Table of Contents

List of Figures

List of Tables

Abbreviations and Notations

Abbreviations:

Abbreviation	Description
1TCM	One-tissue compartment model
2TCM	Two-tissue compartment model
BBB	Blood-brain barrier
CV	Coefficient of variation
CT	Computed tomography
DAT	Dopamine transporter
FDOPA	6-[^{18}F]fluoro-L-dopa
[^{18}F]FP-CIT	N-(3-[^{18}F]fluoropropyl)-2-carboxymethoxy-3-(4-iodophenyl) nortropane
GA	Graphical analysis
GP	Gjedde-Patlak
LLS	Linear least squares
NRE	Non-relative equilibrium
MLAIR	Multiple linear analysis for irreversible radiotracers
MRTM	Multilinear reference tissue model
MRI	Magnetic resonance imaging
PD	Parkinson's disease
PET	Positron emission tomography
RE	Relative equilibrium
ROI	Region of interest
SNR	Signal-to-noise ratio
SPM	Statistical parametric mapping
SRTM	Simplified reference tissue model
TAC	Time-activity curve

Notations for Kinetic Model Equations:[①]

Notation	Description
BP	Binding potential
BP_{F}	In vivo binding potential given as a ratio at equilibrium of specifically bound radioligand in tissue to that of free concentration in plasma (unitless or $\mathrm{mL \cdot cm^{-3}}$)
BP_{ND}	In vivo binding potential given as a ratio at equilibrium of specifically bound radioligand to that of nondisplaceable radioligand in tissue (unitless or $\mathrm{mL \cdot cm^{-3}}$)
BP_{P}	In vivo binding potential given as a ratio at equilibrium of specifically bound radioligand in tissue to that of total concentration in plasma (unitless or $\mathrm{mL \cdot cm^{-3}}$)
$C_{\mathrm{F}}(t)$	Concentration of free (unbound) radioligand in tissue ($\mathrm{kBq \cdot ml^{-1}}$)
$C_{\mathrm{ND}}(t)$	Concentration of nondisplaceable (free and nonspecifically bound) radioligand in tissue ($\mathrm{kBq \cdot ml^{-1}}$)
$C_{\mathrm{NS}}(t)$	Concentration of radioligand nonspecifically bound to other proteins in tissue ($\mathrm{kBq \cdot ml^{-1}}$)
$C_{\mathrm{P}}(t)$	Concentration of unmetabolited parent radioligand in arterial plasma ($\mathrm{kBq \cdot ml^{-1}}$)
$C_{\mathrm{R}}(t)$	Total concentration of radioligand in reference region ($\mathrm{kBq \cdot ml^{-1}}$)
$C_{\mathrm{S}}(t)$	Concentration of radioligand specifically bound to a receptor of interest in tissue ($\mathrm{kBq \cdot ml^{-1}}$)
$C_{\mathrm{T}}(t)$	Total concentration of radioligand in tissue ($\mathrm{kBq \cdot ml^{-1}}$)
$C_{\mathrm{T}}^{*}(t_i)$	Instantaneous measurement at frame time of $C_{\mathrm{T}}(t)$; PET measurement ($\mathrm{kBq \cdot ml^{-1}}$)
DVR	Distribution volume ratio or tissue−to−reference ratio of V_{T} (unitless)

[①] Superscript ' is used for parameters defined in reference region, including rate constants, volumes of distributions, or GA methods' model parameters. Besides, superscript † is used for all parameters obtained from reference−region−based (noninvasive) methods, except for distribution volume ratio (DVR_{Method}).

DVR_{Method}	DVR estimated as the slope parameter in the noninvasive GA method: Logan plot, RE plot, or RE−GP method (unitless)
f_{P}	Free fraction of radioligand in plasma, which is not bound to plasma protein (unitless)
K_1 (or K_1')	Rate constant for delivery of radioligand from arterial plasma to tissue (or to reference region) ($\text{mL} \cdot \text{cm}^{-3}\text{min}^{-1}$)
k_2	Rate constant for efflux of radioligand from tissue to plasma (min^{-1})
$k_{2\text{a}}$	Apparent rate constant for efflux of radioligand from tissue to plasma when the tissue region can be approximately described with one compartment for $t > 0$ (min^{-1})
k_{2a}^{*}	Apparent rate constant for efflux of radioligand from tissue to plasma when the tissue region can be approximately described with one compartment only for $t > t^{*}$ (min^{-1})
k_2'	Apparent rate constant for efflux of radioligand from reference region to plasma when the reference region can be approximately described with one compartment only for $t > t^{*}$ (min^{-1})
$\bar{k}_2'$	A population average of k_2' (min^{-1})
k_3	Rate constants for unbound radioligand's binding to neuroreceptor and release from the neuroreceptor (min^{-1})
k_4	Rate constants for bound radioligand's release from neuroreceptor, (min^{-1})
K_{in} (or K_{in}')	Net influx rate of radioligand from plasma into irreversible compartment in tissue (or in reference region) ($\text{mL} \cdot \text{cm}^{-3} \cdot \text{min}^{-1}$)
$K_{\text{in,GP}}$ (or $K_{\text{in,GP}}'$)	K_{in} (or K_{in}') estimated as the slope parameter in the invasive GP plot ($\text{mL} \cdot \text{cm}^{-3} \cdot \text{min}^{-1}$)
$K_{\text{in,GP}}^{\dagger}$	$K_{\text{in}}/V_{\text{T}}'$ estimated as the slope parameter in the noninvasive GP plot (min^{-1})
t	Post−injection time (min)
t_i	Midpoint of i−th time frame (min)
t^{*}	Time when graphical plot becomes linear (min)
V_{b}	Arterial blood volume fraction (unitless)
V_{ND}	Volume of distribution for nondisplaceable compartment ($\text{mL} \cdot \text{cm}^{-3}$)

V_{NS}	Volume of distribution for nonspecific binding compartment ($mL \cdot cm^{-3}$)
V_S	Volume of distribution for specific binding compartment ($mL \cdot cm^{-3}$)
V_T (or V_T')	Total volume of distribution in tissue (or in reference region) ($mL \cdot cm^{-3}$)
$V_{T,Method}$ (or $V_{T,Method}'$)	V_T (or V_T') estimated as the slope parameter in the invasive GA method: Logan plot, RE plot, or RE−GP method ($mL \cdot cm^{-3}$)
β_{Method} (or β_{Method}')	The intercept parameter for target tissue (or reference tissue) in an invasive GA method: GP plot, Logan plot, RE plot, or RE−GP method
$\beta_{Method}^{\dagger}$	The intercept parameter for target tissue in the noninvasive GA method: GP plot, or RE plot②
$\bar{\beta}_{Logan}'$	A population average of β_{Logan}'

② The intercepts in the noninvasive Logan and RE−GP methods are defined as the intercepts in the corresponding invasive methods (β_{Logan} and β_{REGP}, respectively). Thus, I omit their separate notations.

Chapter 1 Introduction

1.1 Tracer Kinetic Modeling in PET

Tracer kinetic modeling in dynamic positron emission tomography (PET) has played a leading role in quantitative *in vivo* studies on the functional and molecular basis of brain diseases, mainly because of the high sensitivity and quantitative accuracy of PET imaging (*1–5*). Using a tiny amount of radioactive tracer or radioligand injected into the living body, dynamic neuroreceptor PET can accurately capture the temporally changing spatial distribution of the radioligand in the brain, which reflects the targeted receptor's density and dynamic interaction with the radioligand (*6–8*). Nevertheless, the spatiotemporal distribution also contains other distracting information such as the inherent statistical noise associated with radioactive decay, and physiological factors of secondary interest (*3, 7, 9*). The techniques of tracer kinetic modeling, through a mathematical framework, can refine this noisy information from PET data into several quantitative parameters that characterize the receptor distribution and/or the binding process in the brain (*1, 6, 10*). Therefore, in both clinical and basic research, this method has been widely used to investigate the characteristic distribution patterns of neuroreceptors or their dysfunction, which is related to brain diseases, and the effects of new drugs (*11–16*).

1.2 Regional versus Voxel-wise Quantification

Over the last few decades, the practical goal of tracer kinetic modeling in PET has been progressing from an analysis of regional data to a production of images of kinetic-model parameters (*17-19*). The typical procedure of tracer kinetic modeling involves fitting a suitable kinetic model to the tissue time-activity curves (TACs) at the regional or voxel level that are collected from the reconstructed dynamic PET images (*3, 17, 20*).

The regional analysis can be easily performed with lower computational cost and better statistical properties owing to the smaller number of and lower noise-level of the regional TACs that are usually obtained by averaging the voxel TACs within a predefined region of interest (ROI). However, the delineation of ROIs requires prior knowledge of the receptor distribution, and is operator-dependent and time- and labor-consuming when manually done (*5, 8*). More importantly, the results from regional analysis can provide only the average information within a given ROI, and their accuracy is dependent on the size of the ROI.

On the contrary, the analysis of voxel TACs can fully exploit the spatiotemporal information captured in dynamic PET frames, and produce images of kinetic-model parameters that quantitatively characterize the targeted neuroreceptor system (*8, 21*). Furthermore, such parametric images allow the analysis of the entire brain volume

regardless of specific anatomy, such as in voxel-based statistical analysis using the SPM package (Statistical Parametric Mapping, University College of London, UK) (*16, 19, 22*). Therefore, the estimation of parametric images is becoming more preferable, though regional analysis is still important for the exploration of the overall characteristics of tracer kinetics.

Although parametric image generation may cover broad concepts including the voxel-wise measurement of standard uptake values from a single static image, or other standard kinetic parameters such as peak concentration from dynamic data(*5, 8, 23*), it refers to, throughout the thesis, a voxel-wise application of a specific mathematical modeling approaches for dynamic PET images, to obtain images of specific model parameter.

1.3 Requirements for Parametric Imaging

Because of the huge amounts of voxels in dynamic images and high-level noise therein, parametric imaging is more challenging in terms of computational complexity and statistical reliability than ROI-based analysis (*4, 8, 18, 19, 22*). This issue will become more crucial as the resolution of PET images improves or the required injection dose of a radioligand diminishes, based on the advancement of PET scanners (e.g., HRRT (*24*)). Thus, parametric imaging techniques need to be very robust to noise, computationally more efficient, and moreover

user-independent and automatic (*17, 19*).

Conceptually, most kinetic analysis techniques are applicable for the estimations of both regional parameters and parametric images. In practice, however, methods based on nonlinear parameter estimation are undesirable for parametric imaging because of a higher computational burden and less reliability compared with those relying on linear techniques (*8, 21, 22*). Therefore, the use of compartmental analysis, which is a standard kinetic modeling method based on nonlinear estimation, has long been limited mostly to regional data, although it is now being extended to voxel data thanks to recently increased computational power and regularization techniques (*25-28*) that were developed to address the high noise-susceptibility issue. In parametric image generation, instead, more preferable approaches have relied on the linearization of the standard compartment models in various ways so that computationally efficient and reliable linear estimation techniques are applicable.

1.4 Graphical Analysis

One major linearization technique is to integrate the compartment model equations to produce a simple linear regression model that is linear in the parameters (*17*). This method based on the simple model is called graphical analysis (GA), and its parameter estimation depends on a linear estimation technique that has a closed form solution and is

thus computationally simple. Furthermore, this method achieves a level of model independence by fitting only the later portion of the measured data to a simple linear model with only two parameters (*17*), in contrast to the compartment modeling that requires to determine the best model configuration in advance; this fitting strategy enables the use of common properties among the compartmental models (steady state of specific binding). These strengths of the GA method can greatly facilitate the generation of parametric images by enabling simple, reliable and computationally efficient parameter estimation.

1.5 Thesis Statement and Contributions

In this thesis, I focus on GA-based parametric image generation from dynamic neuroreceptor PET data. As introduced previously, thanks to the linearization and simplification of the underlying model, GA methods allow very desirable parametric imaging that is independent of any compartmental model configuration, robust to noise, and computationally efficient. However, both the linearization and simplification depend on several assumptions, violation of which can lead to an inaccurate estimation of parameters of interest (*29-31*). Furthermore, it may end up missing some information or exploiting only fragmentary information from given data because those assumptions are commonly hard to satisfy simultaneously, particularly in parametric imaging for slow kinetic tracers. Therefore, the recent advances in GA

approaches have been mainly based on a reduction of specific assumptions or replacement with new ones.

Meanwhile, a combination of two methods may improve such intrinsic limitation of GA approaches by taking full advantage of the data and also strengths of each GA method. Main contributions of the thesis on this topic, the combination of GA methods, are

1) To provide an overview of recent advances in the parametric mapping of neuroreceptor binding based on GA methods.

2) To suggest a new bi-graphical method without a necessity of blood sampling, in which the parameter of interest can be computed, not directly using linear parameter estimation, but indirectly using the parameters estimates from two other reference-region-based GA approaches.

1.6 Organization of the Thesis

This thesis is organized as follows. Chapter 2 briefly introduces the basic concepts in tracer kinetic modeling for neuroreceptor PET studies, including commonly used compartment models and major parameters of interest. Throughout this thesis, I follow the consensus nomenclature in (*32*). (More detailed concepts and principles of tracer kinetic modeling are presented in numerous studies (*3-5, 7-9, 23, 33, 34*)). Subsequently, Chapter 3 presents an overview GA-based parametric mapping of neuroreceptor binding. Technical details of GA

approaches for reversible and irreversible radioligands are described considering both arterial-plasma-input-based (*invasive*) and reference-region-input-based (*noninvasive*) models. Their statistical properties are discussed in view of parametric imaging. Chapter 4 begins with introducing a conventional invasive bi-graphical approach and proceed to describe how I derived the new noninvasive extension of the approach. Then, I detail the validation of the proposed method using simulation data and its application to human brain PET studies of a slowly binding radioligand. The evaluation results of the statistical properties and its feasibility for human data are presented in the next section, followed by the discussion. Finally, the summary and conclusion are presented in Chapter 5.

Chapter 2 Basic Theory in Tracer Kinetic Modeling

2.1 Dynamic PET Acquisition

In dynamic neuroreceptor PET studies, a very small amount of radioligand with high specific activity, which is designed to follow a substrate physiological and biochemical process of interest without disturbing the associated system, is introduced into the bloodstream of an individual participant (mostly by a single intravenous bolus). The radioligand administrated is delivered to capillaries in the brain by arterial blood flow, subsequently extracted from arterial blood into tissue space across the blood–brain barrier in the capillaries, and finally bound to high-affinity receptors in the tissue through the targeted biochemical process (*9*). Accordingly, the radioligand is differentially accumulated into and cleared from diverse brain tissues over time, depending on the physiological and biochemical properties of the radioligand as well as the target process (*8*).

The characteristic spatiotemporal distribution of the radioligand in the brain can be imaged by a dynamic PET scan in which the radioactivities from the delivered radioligands are counted and then recorded in a series of image frames over irregular time intervals. Although an individual dynamic image represents the average spatial distribution of radioactivities during the corresponding frame duration,

it is usually assumed to be instantaneous at the midpoint of the frame (t_i). After a number of corrections (including a radioactivity−decay correction), reconstruction, and calibration, each dynamic PET image then represents the instantaneous noisy measurement ($C_{\mathrm{T}}^{*}(t_i)$) at the frame time of the time−varying radioligand concentrations in each region, $C_{\mathrm{T}}(t)$, ($\mathrm{kBq}\cdot\mathrm{ml}^{-1}$); t is the post−injection time. Therefore, by collecting the time course of the measurements from each voxel of dynamic PET images (or averaging them over the voxels within a specific ROI), we obtain voxel−wise TACs (or ROI TACs) as $C_{\mathrm{T}}^{*}(t_i)$.

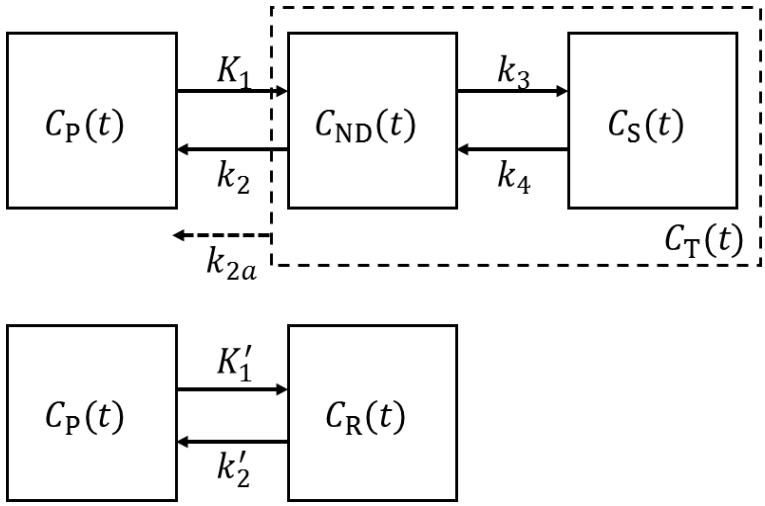

Figure 2.1. Standard two-tissue compartment model (2TCM) for a target region or tissue (top) and one-tissue compartment model (1TCM) for reference region (bottom) to describe the *in vivo* kinetic behavior of neuroreceptor radioligands. Top: concentrations ($\mathbf{kBq \cdot ml^{-1}}$) of radioligands in the same states are represented as compartments: plasma concentration of unmetabolited parent radioligand ($\boldsymbol{C_P}$), that of nondisplaceable (free and nonspecifically bound) radioligand ($\boldsymbol{C_{ND}}$), that of specifically bound radioligand ($\boldsymbol{C_S}$); their exchanges between compartments are explained with the rate constants: $\boldsymbol{K_1}$ ($\mathbf{mL \cdot cm^{-3} min^{-1}}$) and $\boldsymbol{k_2}$–$\boldsymbol{k_4}$ ($\mathbf{min^{-1}}$); and $\boldsymbol{C_T}$ represents the total tissue concentration ($\boldsymbol{C_{NS} + C_S}$). In addition, $\boldsymbol{k_{2a}}$ denotes the apparent efflux rate constant from tissue when the tissue region can be approximately described with one compartment (the dashed box) because of the equilibrium between $\boldsymbol{C_{ND}}$ and $\boldsymbol{C_S}$. Bottom: $\boldsymbol{C_R}$ represents the total concentration in the reference region and $\boldsymbol{K_1'}$ ($\mathbf{mL \cdot cm^{-3} min^{-1}}$) and $\boldsymbol{k_2'}$ ($\mathbf{min^{-1}}$) are the rate constants for their influx and efflux from $\boldsymbol{C_P}$.

2.2 Compartmental Models

The measured PET data can be described with a mathematical model or a comprehensive description of the underlying processes that is developed based on a prior understanding of the kinetic behavior of radioligands in brain tissue (*7–9*). The most widely used one is compartmental model that forms the basis for tracer kinetic modeling in PET (*3, 33*).

With prior knowledge of their expected *in vivo* kinetics, the injected radioligands can be assumed to form a limited number of separate pools, called compartments, according to their physical and chemical states. In general, the concentration of unmetabolited parent radioligand in plasma (C_{P}) ($\mathrm{kBq \cdot ml^{-1}}$) is considered as one compartment because it serves as the input for the radioligands delivered into the tissue. As for the radioligands in the tissue, the following pools are considered as plausible in studies of receptor–ligand bindings: those in free form (C_{F}), those specifically bound to the receptor of interest (C_{S}), and those nonspecifically bound to other proteins (C_{NS}). Then, we have the following relationship:

$$C_{\mathrm{T}}(t) = C_{\mathrm{F}}(t) + C_{\mathrm{NS}}(t) + C_{\mathrm{S}}(t). \tag{2.1}$$

Together with several assumptions, such as homogeneous concentration and instantaneous mixing of radioligands within a compartment, the small injection dose and high specific activity enables the use of first–order rate constants to describe exchanges of

radioligand between compartments (*1, 2, 6, 9, 35*); so, the transport and binding rates of the radioligand are assumed to be linearly related to the concentration differences between compartments. These considerations lead to linear compartment models.

Figure 2.1 (top) depicts the standard two-tissue compartment model (2TCM) that involves only two compartments to represent the radioligand concentration within the tissue and that is commonly used to study neuroreceptor ligand binding. By assuming a rapid equilibrium between free and nonspecifically bound tissue compartments ($C_{\mathrm{F}}(t)$ and C_{NS}), the two compartments can be considered as one unified compartment, called the nondisplaceable compartment (C_{ND}) (*1, 2, 10*). This assumption applies well to most neuroreceptor ligand studies because of the limited temporal resolution and statistical quality of the PET data; usually, the aforementioned model containing three-tissue compartments is in practice too complex to provide reliable results (*3, 10*). In this model, the exchanges of radioligand are described by four rate constants: K_1 ($\mathrm{mL \cdot cm^{-3} min^{-1}}$) is the rate constant for the delivery of the radioligand from arterial plasma to tissue while k_2 ($\mathrm{min^{-1}}$) is the rate constant for its efflux from tissue; and k_3 and k_4 ($\mathrm{min^{-1}}$) are the rate constants for the binding and release from the neuroreceptor, that is, the exchange between $C_{\mathrm{ND}}(t)$ and $C_{\mathrm{S}}(t)$.

For the radioligands showing fast kinetics, i.e., where the binding and release of the radioligand from the receptor is rapid enough and thereby $C_{\mathrm{ND}}(t)$ and $C_{\mathrm{S}}(t)$ are indistinguishable, the model can be further

simplified into one–tissue compartment model (1TCM) (*10, 36*). In this case, the efflux rate constant k_2 is replaced by the apparent one $k_{2a} = k_2/\left(1 + (k_3/k_4)\right)$. Furthermore, the 2TCM is also commonly used for irreversibly binding radioligands whose binding process is intrinsically irreversible or seems to be so during the time period of PET studies. The irreversible accumulation of these radioligands can be analyzed by assuming that $k_4 = 0$.

In compartmental modeling, the final goal is to estimate the rate constants, which characterize the kinetics of the radioligand, from the measured data. Besides the measured PET data $C_T^*(t_i)$, the input function $C_P(t)$ also needs to be measured to obtain the rate constants. The process of measuring $C_P(t)$ generally relies on frequent invasive arterial blood sampling (*37, 38*) under the assumption that the arterial plasma concentration is same as the capillary plasma concentration (*8*); arterial blood samples are measured separately during the dynamic PET acquisition and subsequently are corrected for metabolites since the standard model assumes that no plasma metabolites cross the blood–brain barrier. As the sampling times of blood data are incompatible with dynamic frame times, some simple signal processing may be required to match them. Contrary to the measured tissue data $C_T^*(t_i)$, where t_i is the matched sampling time for the ith measurement, I will also maintain $C_P(t_i)$ without the superscript for the measured input data, because the data are usually refined through plasma input modeling (*39*).

Although the arterial blood sampling method is considered to be the gold standard of measuring $C_P(t)$ based on its accuracy(*8*), it has several disadvantages such as invasiveness and technical demands (*8, 23, 40*). Therefore, to minimize or eliminate the needs of the invasive and technically demanding blood sampling and metabolite correction, the following approaches have been proposed and applied (*40, 41*): image-derived methods (*42-44*), model-based methods (*45-47*), reference region methods (*36, 48-51*) and other sophisticated approaches (*52-58*).

In reference region methods, the kinetics of the radioligand in the tissue is described as a function of reference region data by assuming that there exists a reference area of brain tissue effectively devoid of specific binding sites (*33*). Therefore, they require an additional compartment $C_R(t)$ and related rate constants K_1' ($\mathrm{mL \cdot cm^{-3} min^{-1}}$) and k_2' ($\mathrm{min^{-1}}$) as shown in Figure 2.1 (bottom). As these additions increase the complexity of the model and thus uncertainty in the resulting estimates, a series of assumptions are usually made to reduce the complexity (*21*); 1) nonspecific binding is the same in both areas though delivery is not, and 2) an equilibrium is rapidly achieved between C_{ND} and C_S so that tissue kinetics effectively follow 1TCM.

2.3 Parameters of Interest in Neuroreceptor Study

In studies of *in vivo* reversible neuroreceptor-ligand binding, the

primary outcome is the equilibrium concentration of the radioligand specifically bound to the target receptor (C_S) that reflects the density and affinity of the receptors available to react with the radioligand *in vivo* (*32*). Although separate estimation of the density and the affinity may be more desirable, they are inseparable under the single tracer injection protocol (*6*). Instead, therefore, the concentration of specific radioligand binding is usually quantified as its equilibrium ratio to another pool of radioligand concentration, termed binding potential (BP), which means the product of the receptor density and the binding affinity. In the literature, there has been three different practical definitions of *in vivo* BP depending on the use of distinct normalization factors (or the input measurements): nondisplaceable concentration in tissue (C_{ND}), total concentration in plasma (C_P) or its free fraction ($f_P C_P$) (*32*). These *in vivo* BP definitions represent the potential of available receptors to bind with the radioligand, and reflect the density of available receptors under the assumption that there are no substantial regional changes in receptor affinity.

For consistency in this thesis, however, I will limit myself to $BP_{ND} = C_S(t)/C_{ND}(t)$ (unitless) because only BP_{ND} can be obtained from both the reference region model (usually directly) and from the plasma input model (indirectly) that I will describe. Although the other parameters, $BP_P = C_S(t)/C_P(t)$ and $BP_F = C_S(t)/(f_P C_P(t))$, are considered to be more ideal to describe specific binding than BP_{ND}, the measurement of plasma concentration or its free fraction is necessary to estimate them.

Therefore, BP_{ND} is also frequently used (in a variety of applications) mainly because of practicality. However, the interpretation of BP_{ND} requires careful attention because its use is based on the assumption that nondisplaceable uptake has no regional or group difference; the comparison of BP_{ND} may not clearly reveal the group difference associated with specific binding when it has a group difference or treatment effect (*32, 59*).

Another common endpoint is the volume of distribution of total radioligand concentration in tissue (V_{T}). In the field of *in vivo* imaging, volume of distribution refers to the volume (mL) of plasma (with a certain concentration) required to account for the amount at equilibrium of radioligand in the unit volume ($1\ \mathrm{cm}^3$) of the target region, and is therefore usually represented as the ratio of the radioligand concentration in the target (tissue or compartment) to that in the plasma ($\mathrm{mL}\cdot\mathrm{cm}^{-3}$). Thus, V_{T} has the following relationship with the volume of distribution of each compartment:

$$V_{\mathrm{T}} = \frac{C_{\mathrm{T}}(t)}{C_{\mathrm{P}}(t)} = \frac{C_{\mathrm{ND}}(t)}{C_{\mathrm{P}}(t)} + \frac{C_{\mathrm{S}}(t)}{C_{\mathrm{P}}(t)} = V_{\mathrm{ND}} + V_{\mathrm{S}}, \tag{2.2}$$

where V_{ND} and V_{S} are the volumes of distribution for nondisplaceable and specific binding compartments, respectively.

Though V_{T} does not directly reflect specific binding but rather total radioligand uptake in tissue, it is also widely used in studies of neuroreceptor binding (*60*). Indeed, most graphical analysis using the plasma input function provides V_{T} as a major outcome. Because these

methods yield a V_{ND} estimate for a receptor-free region, BP_{ND} can be indirectly computed as $BP_{ND} = V_T / V_{ND} - 1$. Similarly, even most reference-region-based methods produce estimates of the tissue-to-reference ratio of V_T (V_T/V_{ND}), called the distribution volume ratio (DVR), to derive BP_{ND}. Furthermore, it is noteworthy that the V_S is BP_P in itself; thus, for a tracer with a high level of specific binding and/or a low level of nonspecific binding (e.g. [^{11}C]flumazenil), $V_T (\approx V_T - V_{ND} = V_S)$ can yield a good estimate of the receptor density (*10*).

Meanwhile, the concept of binding potential or volume of distribution is not useful for irreversibly binding radioligands. The major outcome of interest for these radioligands is the influx rate constant (K_{in}, $\mathrm{mL \cdot cm^{-3} \cdot min^{-1}}$) which is the net influx rate of the radioligand from plasma into the irreversible compartment. K_{in} can be directly obtained from graphical analysis using the plasma input function, while only relative values normalized by reference region information such as K_{in}/V'_T or K_{in}/K'_{in} can be acquired from reference region methods (*33*).

The aforementioned parameters can be related to the rate constants of the 2TCM for reversibly binding radioligands as follows (*10*):

$$V_T = \frac{K_1}{k_2}\left(1 + \frac{k_3}{k_4}\right), \tag{2.3}$$

$$V_{ND} = \frac{K_1}{k_2}, \tag{2.4}$$

$$BP_{ND} = \frac{k_3}{k_4} = \frac{V_T}{V_{ND}} - 1. \tag{2.5}$$

Similarly, when the 2TCM can be simplified into 1TCM, we can consider the following relationship:

$$V_{\mathrm{T}} = \frac{K_1}{k_{2a}} = \frac{K_1}{k_2}\left(1 + \frac{k_3}{k_4}\right). \quad (2.6)$$

For a reference region commonly described by the 1TCM (*60, 61*), we have

$$V'_{\mathrm{T}} = V'_{\mathrm{ND}} = \frac{K'_1}{k'_2}. \quad (2.7)$$

Therefore, under the assumption $V_{\mathrm{ND}} = K_1/k_2 = K'_1/k'_2 = V'_{\mathrm{ND}} = V'_{\mathrm{T}}$, reference-region-based methods can provide direct estimation of binding potential, by using reference region data to acquire information about the nondisplaceable component in tissue. Hence, the identification of a reliable reference region effectively devoid of specific binding is crucial (*59*). On the other hand, when modeling the kinetics of irreversible binding radioligands using the 2TCM with $k_4 = 0$, we have

$$K_{\mathrm{in}} = \frac{K_1 k_3}{k_2 + k_3}. \quad (2.8)$$

2.4 Limitations in Parametric Image Generation

Although the standard compartment model describes a linear system, it is not linear in parameters. Therefore, the estimation of parameters in compartment models requires nonlinear estimation techniques. Because of its optimal statistical accuracy and reliability (*62*), the NLS method is considered to be the method of choice for tracer kinetic modeling and is often used as the gold standard to assess the performance of other methods in terms of ROI parameters (*8, 17*).

However, nonlinear fitting approaches have no closed-form solution and are usually solved in an iterative way. This iterative approach yields a tremendous computational burden when applied to voxel-by-voxel analysis. Furthermore, the performance of nonlinear fitting is dependent on the initial guessing of parameters; poor initial values result in finding incorrect optima at local minima of the cost function and slow convergence. In addition, an appropriate convergence threshold and constraints on the parameters should be determined by experience (*5*).

Chapter 3 Overview of Graphical Analysis

3.1 General Characteristics

As briefly introduced in Chapter 1 (Section 1.4), graphical analysis (GA) method is the simplest approach for kinetic parameter estimation, which relies on a linear parameter estimation technique. In some literature, the term 'graphical analysis' has been used to indicate specific early methods such as the Gjedde–Patlak (GP) plot for the quantification of irreversible radioligand uptake (*63–65*) and the Logan plot for reversible radioligand binding (*60, 66*). However, it is now considered as a category rather than a specific method, since several different GA models have also been developed to measure different parameters or to improve other models (*31, 40, 41, 67–69*). Table 3.1 lists the characteristics of all GA methods.

In each GA approach, the kinetic behavior of the radioligand is described by only two variables (for a simple linear regression) that are transformed from the measured data, including an input function, and that establish a linear relationship partially and asymptotically. The slope and intercept of that asymptotic linear portion can be interpreted as physiologically meaningful parameters, such as V_T or K_{in} (*29*). Hence, first the linearity of the relationship is examined graphically by plotting one variable versus the other (which is why it is called graphical analysis; see Figure 3.1) and then the slope and intercept are estimated by fitting a straight line to the specified linear portion via the

Table 3.1. Overview of graphical analysis methods

	Invasive Logan plot	Invasive RE plot	Invasive GP plot	Invasive RE–GP plot	(Invasive) Ito plot	Noninvasive Logan	Noninvasive RE	Noninvasive GP
Binding type	Reversible	Reversible	Irreversible	Reversible	Reversible	Reversible	Reversible	Irreversible
Input function	C_P	C_P	C_P	C_P	C_P	C_R	C_R	C_R
Model equations	Eq. (3.4)	Eq. (3.10)	Eq. (3.14)	Eqs. (3.10), (3.14),(4.1) –(4.3)	Eq. (3.13)	Eq. (3.9)	Eq. (3.12)	Eq. (3.15)[③] or (3.16)[④]
Parameters of interest	V_T	V_T	K_{in}	V_T	V_{ND} and V_T	V_T/V_T'	V_T/V_T'	K_{in}/V_T' (or K_{in}/K_{in}')
Necessity of C_R	Need only to obtain BP_{ND}	Need only to obtain BP_{ND}	No	Need only to obtain BP_{ND}	No (optional for BP_{ND})	Yes	Yes	Yes (or Yes)
Noisy variable including C_T^*	Dependent, independent	None	Dependent	Dependent	Dependent	Both	Dependent	Dependent (or both)
Major effect of noise on LLS estimates	Negative bias (NB)	Variance	High variance (HV)	Variance	High variance	Negative bias	Variance	HV(or NB)
Linearity condition	$\frac{C_S(t)}{C_T(t)} \to const$ (1TCM after t^*)	$\frac{C_T(t)}{C_P(t)} \to const$	$\frac{C_{ND}(t)}{C_P(t)} \to const$	$\frac{C_S(t)}{C_T(t)} \to const$	$\frac{C_S(t)}{C_T(t)} \to const$ (1TCM after t^*)	Logan condition for tissue and reference	RE condition for tissue and reference	Logan for reversible and GP for irreversible
Reference	(*66*)	(*69*)	(*63, 64*)	(*31*)	(*67, 68*)	(*60*)	(*69*)	(*40, 41, 65*)

[③] Model for reference region with reversible kinetics

[④] Model for reference region with irreversible kinetics (Note that this one is not typical graphical analysis.)

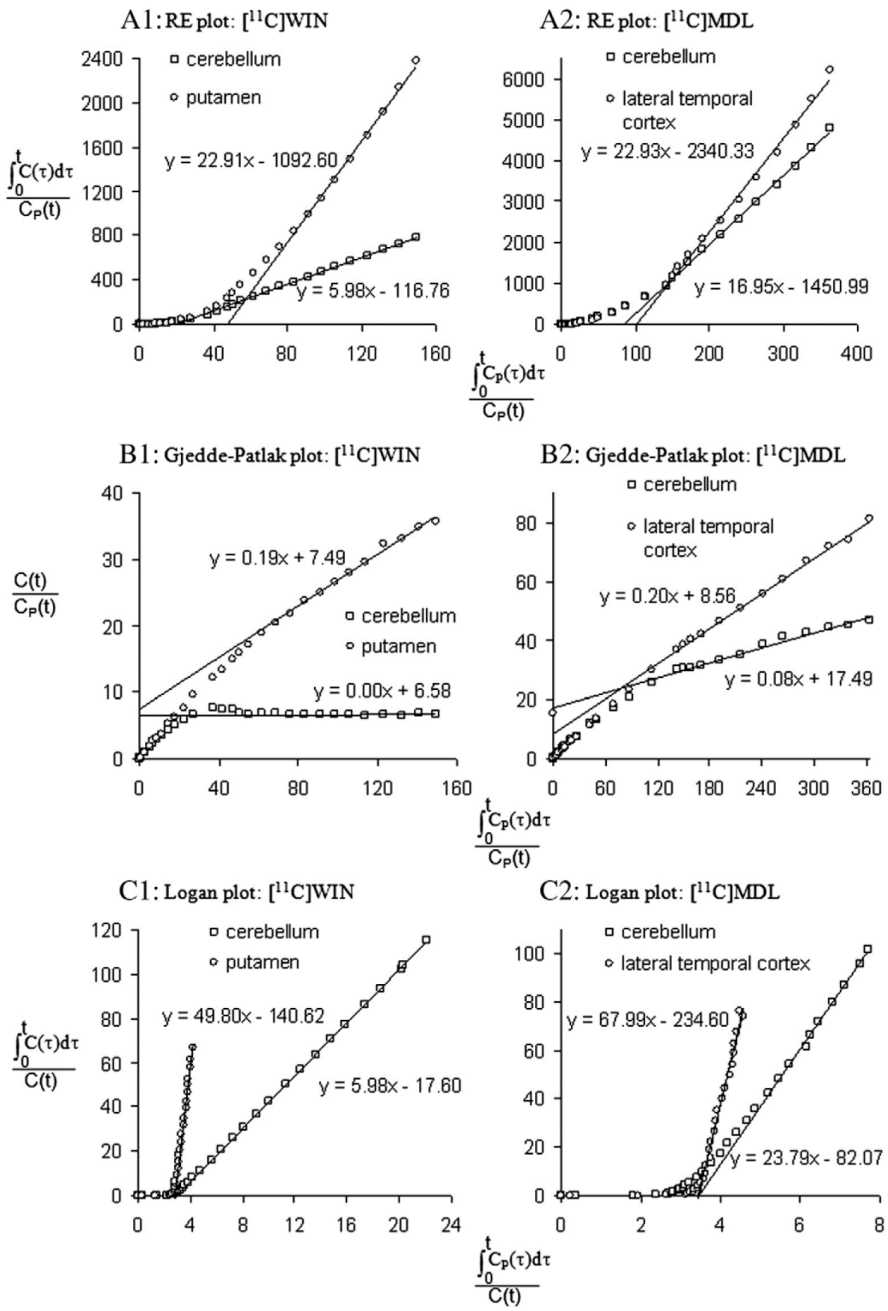

Figure 3.1. Various graphical plots for slow kinetic radiotracers, [^{11}C]WIN and [^{11}C]MDL: (A) RE plot, (B) GP plot, and (C) Logan plot (reprinted from (*31*) with permission).

linear least squares (LLS) method.

To model the linear portion, GA methods rely on a simple linear regression model, or a linear model with a single independent variable, of the following matrix form:

$$\mathbf{y} = \beta_1 \mathbf{x_1} + \beta_0 \mathbf{1} + \boldsymbol{\epsilon} = \mathbf{X}\boldsymbol{\beta} + \boldsymbol{\epsilon}, \tag{3.1}$$

where $\mathbf{y}$ and $\mathbf{x_1}$ are $n \times 1$ vectors of dependent and independent variables, respectively; $\mathbf{X} = [\mathbf{x_1}, \mathbf{1}]$ is an $n \times 2$ matrix of the $\mathbf{x_1}$ and all−ones vector ($\mathbf{1}$) for the intercept term; $\boldsymbol{\beta} = [\beta_1, \beta_0]^T$ is a vector of 2 parameters including the slope (β_1) and the intercept (β_0); and $\boldsymbol{\epsilon} = [\epsilon_1, \cdots, \epsilon_n]^T$ is an $n \times 1$ vector of the error term. Then, the slope (β_1) and the intercept (β_0) characterizing the linear portion are usually obtained by solving the LLS problem:

$$\min_{\boldsymbol{\beta}} \|\mathbf{X}\boldsymbol{\beta} - \mathbf{y}\|_2^2, \tag{3.2}$$

which has the following closed form solution or the LLS estimator:

$$\widehat{\boldsymbol{\beta}}_{\mathrm{LLS}} = (\mathbf{X}^T\mathbf{X})^{-1}\mathbf{X}^T\mathbf{y}. \tag{3.3}$$

The GA methods have several advantages that are mainly attained by linearizing compartment model equations into the simple linear model so that the LLS approach can be used (*29, 31*). Both the simplicity of the model and the closed−form solution of the LLS method enable simple, reliable and computationally efficient parameter estimation. Furthermore, in contrast to standard compartmental modeling, the GA methods are consistently applicable across different tissue data with no *a priori* knowledge on the best model structure for each tissue, because their model equations are derived from a general

multi-compartment model in which an arbitrary number of compartments is assumed (*64, 66*). These strengths of GA methods can greatly facilitate the generation of parametric images in which numerous voxels covering various brain regions can be analyzed.

However, a series of assumptions underlie the linearization and simplification of kinetic models for GA that allows the use of simple linear regression and thus provide various advantages. First, GA methods require the determination of t^*, the time when the plot becomes linear, because the linearity of each model is valid only for the later part of the dynamic frames. A poor determination can yield erroneous estimates by violating the linearity requirement. In addition, slow kinetic tracers have a late starting point of the linear portion that requires a longer scan duration or reduces the amount of data available for estimation. Thus, the results can suffer from higher uncertainty because of limited data. Moreover, unbiased parameter estimation in the simple linear regression depends on basic assumptions of LLS: that there are no or negligible errors in the independent variable of the linear model, and that the independent variables are uncorrelated with the error term. Any violation of these conditions can lead to inaccurate results.

Because most PET radioligands bind reversibly, reversible radioligand models have been used more extensively (*1, 70*). Therefore, though most of them were extended from the GP plot for an irreversibly binding radioligand (the first GA method), I introduce the

reversible radioligand models first. Throughout the thesis, 'invasive' (or 'noninvasive') method refers to plasma-input-based (or reference-region-based) method.

3.2 Reversible Radioligand Models

3.2.1 Logan Plot

The Logan plot (Figure 3.1) is a representative GA method used to analyze a reversible radioligand-receptor binding (*60, 66*). The model equation using the plasma input function (*60*) is given by

$$\frac{\int_0^t C_{\mathrm{T}}(s)ds}{C_{\mathrm{T}}(t)} = V_{\mathrm{T,Logan}}\frac{\int_0^t C_{\mathrm{P}}(s)ds}{C_{\mathrm{T}}(t)} + \beta_{\mathrm{Logan}} \text{ for } t > t^*, \tag{3.4}$$

where $V_{\mathrm{T,Logan}}$ is the total distribution volume, and t^* is the time when the intercept β_{Logan} becomes effectively constant. Given the measured noisy TAC, $C_{\mathrm{T}}^*(t_i)$ $(1 \le i \le n)$, obtained from n sequential dynamic frames, we have $y_i = \int_0^{t_i} C_{\mathrm{T}}^*(s)ds / C_{\mathrm{T}}^*(t_i)$, $x_{1i} = \int_0^{t_i} C_{\mathrm{P}}(s)ds / C_{\mathrm{T}}^*(t_i)$, and $\boldsymbol{\beta} = [V_{\mathrm{T,Logan}}, \beta_{\mathrm{Logan}}]^T$ for $1 \le i \le n$. y_i and x_{1i} are ith elements of $\mathbf{y}$ and $\mathbf{x_1}$, respectively. Here, $\int_0^{t_i} C_{\mathrm{T}}^*(s)ds$ represents the numerical integration of $C_{\mathrm{T}}^*(t_i)$ that are discrete-sample data, not the integral of a continuous function.

As other GA methods, the invasive Logan plot is consistently applicable to data from different voxels or ROIs regardless of their underlying model configurations. However, if a particular model configuration is assumed for the given data, $V_{\mathrm{T,Logan}}$ and β_{Logan} can be

related to the specific rate constants included in that configuration; usually the 1TCM or the 2TCM are considered for receptor–ligand studies. The slopes are differently interpreted as Equations (2.3) or (2.7) according to the model configurations. For the 1TCM (without k_3 and k_4), the linearity is simply met for all the frame times (or for $t > 0$) since $\beta_{\mathrm{Logan}} = -1/k_2$. On the contrary, for the 2TCM, we have to determine t^* because the intercept is not actually a constant:

$$\beta_{\mathrm{Logan}} = -\frac{1}{k_2}\left(1 + \frac{k_3}{k_4}\right) - \frac{1}{k_4}\frac{C_{\mathrm{S}}(t)}{C_{\mathrm{T}}(t)}. \tag{3.5}$$

The limit value of the intercept ($-1/k_{2a}^*$) is defined at the steady state condition of tissue tracer kinetics ($\mathrm{d}C_{\mathrm{ND}}(t)/\mathrm{d}t = 0$ & $\mathrm{d}C_{\mathrm{S}}(t)/\mathrm{d}t = 0$):

$$\beta_{\mathrm{Logan}} \to -\frac{1}{k_2}\left(1 + \frac{k_3}{k_4}\right) - \frac{1}{k_4}\frac{k_3}{k_3 + k_4} = -\frac{1}{k_{2a}^*}. \tag{3.6}$$

However, the constancy of β_{Logan} (therefore, the linearity of the model equation) can be approximately achieved before the steady state, in particular, when the tissue kinetic approximately follows 1TCM (that is, at the steady state of specific binding, $\mathrm{d}C_{\mathrm{S}}(t)/\mathrm{d}t = 0$) after t^* (*31, 68*), yielding a good estimate of $V_{\mathrm{T,Logan}}$ (*29, 66, 71*). Therefore, k_{2a}^* can be seen as the apparent efflux rate constant from the apparent single tissue compartment to plasma for $t > t^*$ (min^{-1}). Notice that k_{2a}^* is different from the aforementioned apparent efflux rate constant $k_{2\mathrm{a}} = k_2/\left(1 + (k_3/k_4)\right)$ (see Section 2.2 or Equation (2.6)), which can be defined for $t > 0$; actually, k_{2a}^* represents the sum of $1/k_{2\mathrm{a}}$ and the additional term involving k_3 and k_4 as shown in Equation (3.6). Sufficiently large k_3 and k_4, which allow 2TCM to be approximated

with 1TCM for $t > 0$, would make the additional term negligible compared to k_{2a} and, thus k_{2a}^{*} would become k_{2a}.

Meanwhile, the Logan equation can be re-written for a reference region:

$$\frac{\int_0^t C_R(s)ds}{C_R(t)} = V'_{T,Logan}\frac{\int_0^t C_P(s)ds}{C_R(t)} + \beta'_{Logan} \text{ for } t > t^{*}. \quad (3.7)$$

Rearranging Equation (3.7) gives

$$\int_0^t C_P(s)ds = \frac{1}{V'_{T,Logan}}\left(\int_0^t C_R(s)ds - \beta'_{Logan}C_R(t)\right). \quad (3.8)$$

Then, by approximating the plasma integral in Equation (3.4) using Equation (3.8), the noninvasive Logan plot, based on a reference TAC, can be obtained as follows:

$$\frac{\int_0^t C_T(s)ds}{C_T(t)} = \frac{V_{T,Logan}}{V'_{T,Logan}}\left(\frac{\int_0^t C_R(s)ds - \beta'_{Logan}C_R(t)}{C_T(t)}\right) + \beta_{Logan}. \quad (3.9)$$

Given an ideal reference region devoid of receptor sites, BP_{ND} can be determined as $V_{T,Logan}/V'_{T,Logan} - 1$ under the assumption that $K_1/k_2 = K'_1/k'_2$.

If the reference region is ideal, we also have $\beta'_{Logan} = -1/k'_2$. However, there are several neuroreceptor radioligands whose kinetics in candidate reference regions are best described by 2TCM because of slow nonspecific binding or considerable specific binding in those regions, or etc (*60, 72-75*). Even in those cases, a constant intercept β'_{Logan} may be obtained using the invasive Logan plot, and will be actually determined by not only k'_2 but also additional term (see Equation (3.6)). Nevertheless, in those cases, I will maintain the

expression of $\beta'_{\mathrm{Logan}} = -1/k'_2$ for simplicity; in other words, hereafter, k'_2 will represent the apparent efflux rate constant (from reference tissue to plasma) for $t > t^*$ in the reference region, instead of the actual efflux rate constant (from nondisplaceable compartment to plasma). Notice that, in an ideal reference region, the apparent efflux rate constant becomes the actual efflux rate.

There are several tips for technical efficiency in the implementation of the noninvasive Logan plot. The slope in Equation (3.9), the DVR, may be stably estimated by using a pre-estimated population average of β'_{Logan}, $\bar{\beta}'_{\mathrm{Logan}}$, (or the more physiologically meaningful $\bar{k}'_2$) in place of the individual β'_{Logan} (or k'_2). In this case, the inter-subject variability in β'_{Logan} is blended into an error term of the model and then removed by the fitting process. In addition, the term $\left(\beta'_{\mathrm{Logan}} C_{\mathrm{R}}(t)\right)/C_{\mathrm{T}}(t)$ can be ignored when it is relatively small or becomes constant (*60*); in fact, the term is merged into the error or the intercept term. It is noteworthy that, although the term in parenthesis in Equation (3.9) is treated as one independent variable in the noninvasive Logan plot method, it can be used as two separate variables for the parameter estimation (*76*) that requires multiple linear regression analysis.

Because of its diverse merits, such as model independence, computational efficiency, simple implementation, and statistical reliability under low-noise data, the Logan plot has been extensively used in neuroreceptor-binding studies. However, the invasive or

noninvasive Logan plot suffers from a crucial limitation, especially in parametric imaging (Figure 3.2), in that it produces a severe negative bias in $V_{\mathrm{T,Logan}}$ or $V_{\mathrm{T,Logan}}/V'_{\mathrm{T,Logan}}$ when $C_{\mathrm{T}}(t)$ is highly contaminated (*77–79*). As shown in Equations (3.4) and (3.9), the noise in $C_{\mathrm{T}}(t)$ is entered into both the independent and dependent variables of its model equation while establishing a correlation between them, which therefore makes the model violate the LLS assumptions mentioned in Section 3.1. Furthermore, the magnitude of the bias depends on the noise level that is also dependent (but not linearly) on the radioactivity concentration (*77–80*). The effect of noise is also not consistent throughout the parametric image space; high–binding regions usually undergo more severe underestimation. One minor disadvantage of the Logan plot is the requirement of full dynamic scanning to compute $\int_0^t C_{\mathrm{T}}(s)ds$, though only the later parts of the measurements (after t^*) are used for parameter estimation.

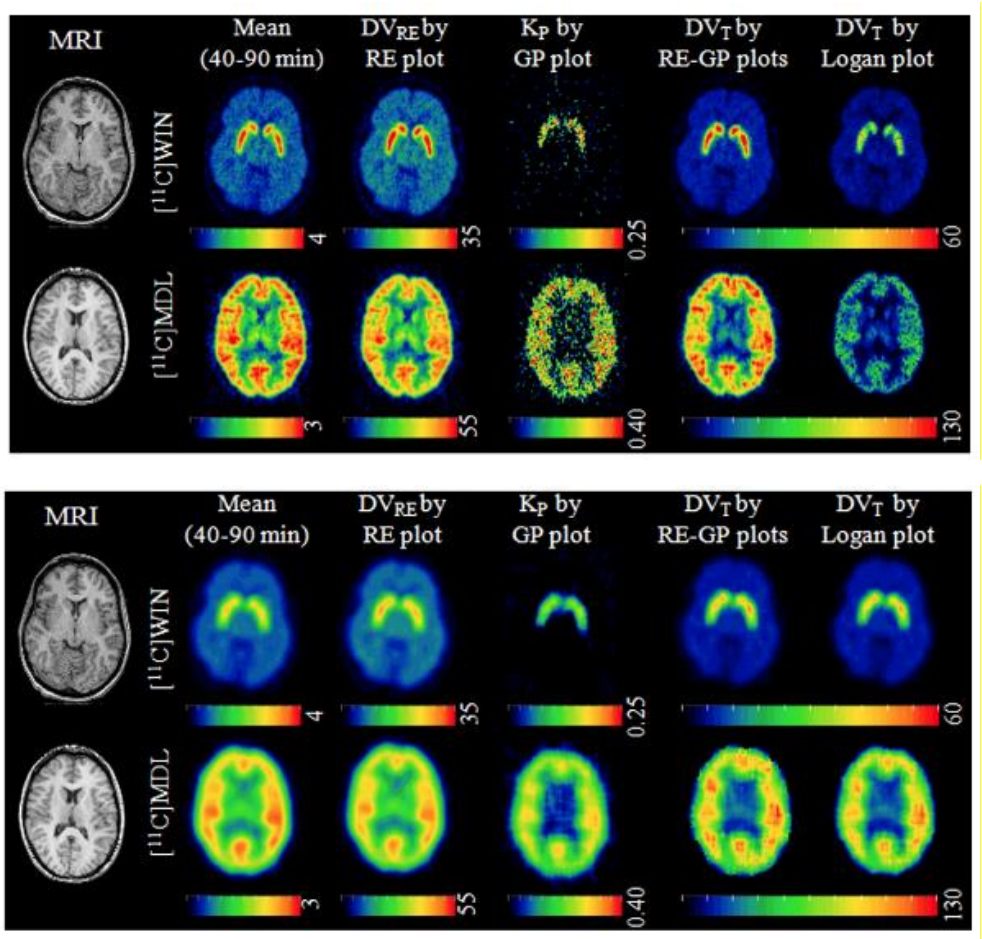

Figure 3.2. Top: parametric images of V_T (represented as DV_{RE} or DV_T) and K_{in} (represented as K_P) from various methods: RE plot, RE−GP plot, and Logan plot (reprinted from (*31*) with permission). Bottom: results from denoised dynamic images (reprinted from (*31*) with permission).

3.2.2 Relative Equilibrium-based Graphical Plot

To address the noise-dependent bias issue in the Logan plot, the relative equilibrium-based graphical method (RE plot; Figure 3.1) was developed for both plasma and reference tissue input functions (*69*). When the tissue to plasma concentration ratio, $C_{\mathrm{T}}(t)/C_{\mathrm{P}}(t)$, becomes a constant, i.e., the relative equilibrium (RE) state established after a certain time t^* (Figure 3.3 left), tracer concentrations satisfy the following relationship:

$$\frac{\int_0^t C_{\mathrm{T}}(s)ds}{C_{\mathrm{P}}(t)} = V_{\mathrm{T,RE}}\frac{\int_0^t C_{\mathrm{P}}(s)ds}{C_{\mathrm{P}}(t)} + \beta_{\mathrm{RE}} \text{ for } t > t^*. \quad (3.10)$$

This model can be derived from compartment model equations or by multiplying the invasive Logan plot model (Equation (3.4)) by $C_{\mathrm{T}}(t)/C_{\mathrm{P}}(t)$. Notice that the constant ratio of tissue-to-plasma concentrations can be achieved at the steady state, but it is also possible to achieve it earlier than the steady state. However, this generally requires somewhat longer times than the Logan linearity condition ($C_{\mathrm{S}}(t)/C_{\mathrm{T}}(t) \rightarrow const$) (*29*).

In addition, when a reference region is also in the RE state for $t > t^*$ ($C_{\mathrm{R}}(t)/C_{\mathrm{P}}(t) = r$), Equation (3.10) can be re-arranged as follows:

$$\int_0^t C_{\mathrm{P}}(s)ds = \frac{1}{V'_{\mathrm{T,RE}}}\left(\int_0^t C_{\mathrm{R}}(s)ds - \beta'_{\mathrm{RE}}C_{\mathrm{P}}(t)\right), \quad (3.11)$$

where $V'_{\mathrm{T,RE}}$ and β'_{RE} are the slope and intercept of the invasive RE plot in the reference region. Then, the following noninvasive RE plot (*69*) can be derived by substituting Equation (3.11) for the plasma integral

in Equation (3.10):

$$\frac{\int_0^t C_{\mathrm{T}}(s)ds}{C_{\mathrm{R}}(t)} = \frac{V_{\mathrm{T,RE}}}{V'_{\mathrm{T,RE}}}\frac{\int_0^t C_{\mathrm{R}}(s)ds}{C_{\mathrm{R}}(t)} + \frac{1}{r}\left(\beta_{\mathrm{RE}} - \frac{V_{\mathrm{T,RE}}}{V'_{\mathrm{T,RE}}}\beta'_{\mathrm{RE}}\right). \qquad (3.12)$$

As the noninvasive Logan plot, the noninvasive RE plot can provide BP_{ND} if the non−receptor region is used for the reference region; however, β'_{Logan} or β'_{RE} is not involved in the independent variable of the RE plot model, making the method be unaffected by inaccurately pre−estimated β'_{Logan} or β'_{RE}.

One merit of the invasive or noninvasive RE plot is its high computational efficiency. As shown in Equations (3.10) and (3.12), each independent variable is not dependent on the tissue data and is common over all voxel TACs. Therefore, once $\mathbf{X}$ ($x_{1i} = \int_0^{t_i} C_{\mathrm{P}}(s)ds/C_{\mathrm{P}}(t_i)$ or $\int_0^{t_i} C^*_{\mathrm{R}}(s)ds/C^*_{\mathrm{R}}(t_i)$) is computed from the input function, it can be used for all tissue data, that is, only one matrix conversion is required for parametric image generation. However, in the case of the Logan plot, $\mathbf{X}$ needs to be computed and inverted for every voxel. In addition, it is noteworthy that both independent and dependent variables in Equations (3.10) and (3.12) have a much lower noise level compared with $C^*_{\mathrm{T}}(t)$ because the integration reduces fluctuations in the later part of TAC, and $C_{\mathrm{R}}(t)$ is obtained by averaging voxel TACs over a reference ROI. Therefore, the RE plot can achieve effectively unbiased estimation with low variance provided that a linearity is established. However, for the linearity, tissue tracer kinetics must be at the RE state during PET scans and only late data

points can be used for the estimation. Thus, good precision properties obtained from a less noisy dependent variable could be compromised with the data reduction because of the relatively late t^*.

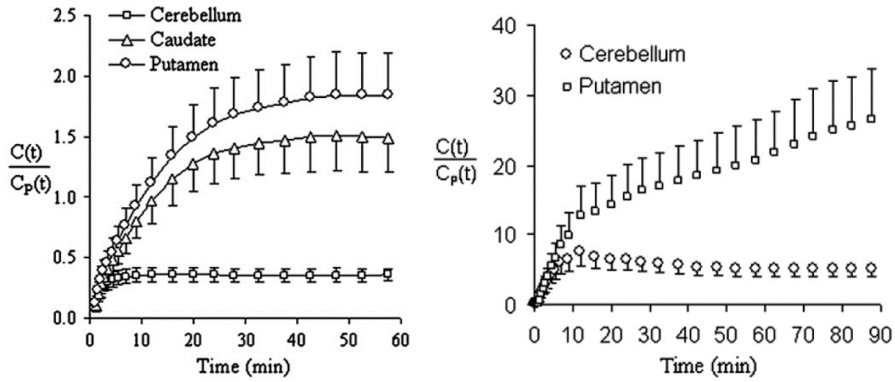

Figure 3.3. Left: relative equilibrium (RE) state after $t^* = 42.5$ min in [^{11}C]raclopride PET (reprinted from (*69*) with permission). Right: violation of RE condition in [^{11}C]WIN PET (reprinted from (*31*) with permission).

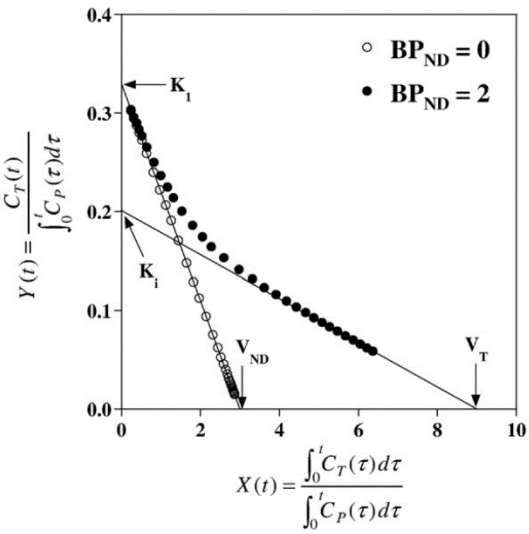

Figure 3.4. An illustration of the Ito plot analysis. The $y-$ and $x-$ intercepts of the regression line represent K_1 and V_{ND}, respectively, for early data frames whereas $K_i = k_{2a}^* V_T$ and V_T for the late part of the data (after the equilibrium time) (reprinted from (*68*) with permission). Open (or filled) circles display examples of applications for one- (or two-) tissue compartment model data.

3.2.3 Ito Plot

Ito et al. (*68*) developed a sort of bi−graphical analysis, where the Yokoi plot (*67*) is applied to the early part of the data frames and the later part separately and then the resulting parameters from both the separate applications are combined to generate BP_{ND}, the parameter of interest. The Yokoi plot was originally proposed to estimate the cerebral blood flow (K_1) and the total distribution volume (V_{T}) only for the tracers well described by the 1TCM. It was recently generalized into the Ito plot (*68*) for the neuroreceptor−radioligand binding studies where the 2TCM is involved. The Yokoi plot and thus the Ito plot rely upon the following linear relationship:

$$\frac{C_{\mathrm{T}}(t)}{\int_0^t C_{\mathrm{P}}(s)ds} = \beta_1 \frac{\int_0^t C_{\mathrm{T}}(s)ds}{\int_0^t C_{\mathrm{P}}(s)ds} + \beta_0 \text{ for } t > t^* \text{ or } t \to 0. \qquad (3.13)$$

The above Equation (3.13) yields a straight line through whole data frames (Figure 3.4) when there is no specific binding in a target region (e.g., the Yokoi plot for 1TCM configuration tracers), and the slope (β_1), y−intercept (β_0), and x−intercept (β_0/β_1) of the regression line represent $-k_2$, K_1, and $V_{\mathrm{T}}(= V_{\mathrm{ND}})$, respectively. On the contrary, when applied to regions with specific binding (e.g., the Ito plot for 2TCM tracers), Equation (3.13) generates a curve (Figure 3.4) that reflects the dynamic effect of specific binding concentration on the measured tissue data. The fitted regression line can be characterized by $-k_2$ (slope), K_1 (y−intercept), and V_{ND} (x−intercept) for the early part of the curve (for $t \to 0$) in which $C_{\mathrm{ND}}(t)$ dominates the measured tissue

concentration $C_T(t)$. The line can also be specified by $-k_{2a}^*$, $k_{2a}^* V_T$ and $V_T (= V_{ND} + V_S)$, respectively, for late-part data ($t > t^*$) that can be approximately described with the 1TCM and its apparent rate constants $k_{2a}^* V_T$ (for influx) and k_{2a}^* (for efflux) after t^* (*31, 68*); k_{2a}^* becomes k_{2a} (Figure 2.1 and Equation (2.6)) when rapid equilibrium is established at $t^* \approx 0$ owing to relatively large k_3 and k_4. Care should be taken in V_{ND} estimation because the use of more data points increases not only the reliability of estimation but also the bias due to the violation of $C_T(t) \approx C_{ND}(t)$ for $t \to 0$ (*81*).

Based upon the plot characteristics that vary according to the model configuration, the Ito plot model (Equation (3.13)) can be useful for graphically distinguishing whether a target region is devoid of specific binding or not (*68*). Furthermore, the Ito plot can be used to compute BP_{ND} using the resulting V_{ND} and V_T estimates. The major distinction between this and other reference region methods is no requirement for *a priori* knowledge of the reference region. These features may be obtained with the invasive Logan plot because the Ito plot and the Logan plot are based on the same linear relationship except for the different arrangement of parameters and variables (thereby, different noise characteristics). Notice that the Yokoi plot and the Ito plot are both invasive graphical analysis techniques for V_T estimation, even though I introduced, at the beginning of this subsection, them as bi-graphical analysis methods for BP_{ND} estimation. In this sense, invasive graphical methods to estimate V_T can also be viewed as a bi-graphical technique

when they are applied to target and reference regions separately to obtain BP_{ND} estimates.

On the other hand, the main drawback of the Yokoi and Ito plots is that the precision of estimates is usually low because of noise effects (*68, 70, 81*), particularly at the voxel-level, for several reasons: 1) the dependent variable includes $C_T(t)$, the major source of noise in kinetic modeling, as its numerator; 2) the estimation of V_{ND} involves early time frames, usually with very low SNR (*8*); and 3) the parameters of interest, V_T and V_{ND}, are computed by dividing the y-intercept by the slope. Therefore, the denoising of dynamic images is inevitable to improve the SNR of parametric images (*8, 81*).

3.3 Irreversible Radioligand Models

3.3.1 Invasive Gjedde–Patlak Plot

For a tracer with an irreversible binding, the Gjedde–Patlak (GP) plot (*63–65*) (Figure 3.1) has been widely used. Although the term 'Patlak plot' or simply 'graphical analysis' is often used for this method, I will keep the 'GP plot' throughout the thesis for consistency with other methods that will be introduced.

The model equation including the plasma input function (Equation (3.14)) can be obtained from the 2TCM by assuming $k_4 = 0$ as well as from a general multi–compartment model (*64, 66*). When an equilibrium has been established between the plasma and reversible components (or $C_{\mathrm{ND}}(t)/C_{\mathrm{P}}(t)$ becomes effectively constant) for $t > t^*$, the following linear model achieves an asymptotic linearity for an irreversibly binding tracer:

$$\frac{C_{\mathrm{T}}(t)}{C_{\mathrm{P}}(t)} = K_{\mathrm{in,GP}} \frac{\int_0^t C_{\mathrm{P}}(s)ds}{C_{\mathrm{P}}(t)} + \beta_{\mathrm{GP}} \text{ for } t > t^*, \tag{3.14}$$

where the influx rate constant $K_{\mathrm{in,GP}} = K_1 k_3/(k_2 + k_3)$ and the intercept term $\beta_{\mathrm{GP}} = (k_2/(k_2 + k_3))(C_{\mathrm{ND}}(t)/C_{\mathrm{P}}(t))$. Thus, β_{GP} has a positive value in contrast with its equivalents in the Logan or RE plots.

In addition to the common advantages of GA methods, the GP plot has a discriminative one in that it does not require a full dynamic scan because the integration of $C_{\mathrm{T}}(t)$ is not involved, in contrast to other methods such as the Logan plot or the RE plot. Furthermore, it is

noteworthy that the GP plot has very similar model equation with the RE plot (Equation (3.10)), except for how $C_T(t)$ is involved in a dependent variable. Therefore, the two methods share similar bias properties and computational efficiency owing to using the same independent variable. On the other hand, the variance of the parameter estimate from the GP plot is more sensitive to noise (Figure 3.2) than that from the RE plot because $C_T(t)$ (i.e., more noisy data) is directly involved in the dependent variable of the GP plot, while its integration (i.e., less noisy data) is used in the RE plot. This noise sensitivity of the GP plot can be improved through multiple linear analysis for irreversible radiotracers (MLAIR) methods (*22*). Moreover, for the tracer assumed to have effectively irreversible binding ($k_4 \approx 0$) over the scan duration, $K_{in,GP}$ may be underestimated if the dissociation of bindings are appreciable (*8*); in such case, a more general model equation is required to obtain unbiased results (*65*).

3.3.2 Noninvasive Gjedde–Patlak Approaches

Concerning the reference region model, the GP plot has two different model equations according to the tracer's binding type in the reference region. When the reference region has only reversible binding sites, the relationship between $C_P(t)$ and $C_R(t)$ can be represented with the Logan plot equation with a slope $V'_{T,Logan}$ and an intercept β'_{Logan} ($\text{for } t > t^*$). Then, by multiplying both sides of Equation (3.14) by

$C_P(t)/C_R(t)$ and substituting Equation (3.8) into Equation (3.14), a noninvasive GP plot model can be obtained as follows:

$$\frac{C_T(t)}{C_R(t)} = \frac{K_{in,GP}}{V'_{T,Logan}} \frac{\int_0^t C_R(s)ds}{C_R(t)} + \left\{ \frac{C_P(t)}{C_R(t)} \beta_{GP} - \frac{K_{in,GP}}{V'_{T,Logan}} \beta'_{Logan} \right\}. \quad (3.15)$$

Thus, the slope and the intercept terms can be estimated using simple linear regression when $\beta_{GP}\, C_P(t)/C_R(t)$ ($\propto C_{ND}(t)/C_R(t)$) and β'_{Logan} become effectively constant for $t > t^*$ (*29, 65*).

Meanwhile, for a reference region with irreversible uptake, the invasive GP equation is used to describe $C_P(t)$ using $C_R(t)$. Then, another linear model of a noninvasive GP plot can be obtained as follows (*40, 41*),

$$\int_{t^*}^t C_T(s)ds = \frac{K_{in,GP}}{K'_{in,GP}} \int_{t^*}^t C_R(s)ds + \frac{\beta_{GP}}{K'_{in,GP}} [C_R(t) - C_R(t^*)] - \frac{\beta'_{GP}}{K'_{in,GP}} [C_T(t) - C_T(t^*)] \text{ for } t > t^*, \quad (3.16)$$

where $K'_{in,GP}$ and β'_{GP} are the slope and intercept of the invasive GP plot applied to the reference region. This method requires that the kinetics of the radioligand in both the tissue and reference regions can be modeled using the invasive GP plot (Equation (3.14)).

The former noninvasive model would inherit all the properties of the original invasive GP plot model, provided that a sufficiently large ROI size is used so as to obtain $C_R(t)$ with as low noise-level as that of $C_P(t)$; otherwise, the accuracy of the resulting estimates can be damaged by the noisy independent variable, like in the Logan plot. On the contrary, the latter noninvasive model has several distinct features

compared with the original invasive and the former noninvasive models. First, this model is not a simple linear regression model but a multiple linear regression model. Therefore, a graphical plot with a straight-line fit is not provided; although the visualization of 3-dimensional hyper-plane fit is possible instead, its interpretation is not as straightforward as that of graphical analysis. In addition, this model includes the integration of $C_T(t)$ in contrast to the others. Nevertheless, it also avoids the requirement of a full dynamic scan like the others; this property of the original GP plot model is just transformed into the integration from t^* to t.

One drawback of these noninvasive methods is that the net accumulation of radioligand is acquired only in a relative or normalized form. Nevertheless, the former noninvasive model has found applications because of its history going back to 1985; the method has been frequently used in 6-[^{18}F]fluoro-L-dopa (FDOPA) studies because of a good correlation between its own results and those from the invasive counterpart (*82-85*). However, the latter method was introduced in relatively recent years and thus has not been sufficiently investigated or used, and has been applied only to ROI data. Although the ROI results have shown good accuracy and precision, future parametric imaging may suffer from severe underestimation because $C_T(t)$ is used for independent variables.

Chapter 4 Noninvasive Bi-graphical Analysis for the Quantification of Slowly Reversible Radioligand Binding

4.1 Background

Each GA approach relies on a series of assumptions for the linearization and simplification of underlying kinetic models that allow the use of simple linear regression and thus provide various advantages. Any violation of those assumptions can lead to an inaccurate estimation of parameters of interest (*29-31*). Besides the linearity condition for later parts of data points, the Logan plot requires that the tissue TAC, which is included in the independent variable of the underlying model, should be noiseless for unbiased LLS estimation of V_T or DVR (*32*). However, this assumption is impractical in a voxel-by-voxel estimation of these parameters, leading to the generation of noisy and biased parametric images because of the high-level noise at the individual voxel level (*77-79*). Conversely, the RE plot (*69*), which is able to address the bias issue in Logan plot, demands that the tracer distribution in tissue attains an equilibrium relative to the input function, the RE state; however, tracers with slow kinetics cannot easily reach the RE state during PET scan as shown in Figure 3.3 (right), causing biases in the results of the RE plot (*31*).

Recently, a bi-graphical analysis method named 'RE-GP plots',

which relies on the plasma input function, has been proposed for the quantification of a reversible tracer binding that may not reach the RE state during PET scans because of its slow binding kinetics (*31*). In the plasma-input-based (invasive) RE-GP method, the slope of the invasive Logan plot, V_T, is obtained indirectly through arithmetic combination of the parameters of the invasive RE and GP plots. The RE and GP parameters require no assumption of noiseless tissue TAC in contrast with the Logan plot. Furthermore, the use of the GP parameters compensates for the bias in RE parameters, which is caused by the violation of the RE condition. Thus, the original RE-GP yields much less bias than the Logan and RE plots.

However, the original RE-GP requires an arterial blood sampling that should be avoided if possible because of its invasiveness and technical demands, and would cause more problems in a long-duration PET scan for slow kinetic tracers, such as a dopamine transporter imaging radioligand, N-(3-[^{18}F]fluoropropyl)-2-carboxymethoxy-3-(4-iodophenyl) nortropane ([^{18}F]FP-CIT) (*86*). Therefore, I undertook to devise a reference-region-based (noninvasive) extension of the invasive RE-GP. In this method, the slope of the noninvasive Logan plot, DVR, is computed indirectly from the parameters of the noninvasive RE and GP plots and the effective efflux rate constant from the reference region to plasma (k_2').

This chapter is organized as follows. I first introduce the invasive RE-GP in detail and then describe how I derived the noninvasive RE-

GP method. Then, I detail the validation of the proposed method using simulation data and its application to human brain PET studies of [^{18}F]FP−CIT, a slowly binding radioligand. The evaluation results of the statistical properties and its feasibility for [^{18}F]FP−CIT are presented in the next section. The discussion follows in the remaining section.

4.2 Materials and Methods

4.2.1 Invasive RE−GP Plots

The invasive RE−GP method (*31*) is based on the following equation,

$$\frac{\int_0^t C_{\mathrm{T}}(s)ds}{C_{\mathrm{T}}(t)} = V_{\mathrm{T,REGP}}\frac{\int_0^t C_{\mathrm{P}}(s)ds}{C_{\mathrm{T}}(t)} + \beta_{\mathrm{REGP}} \text{ for } t > t^*, \tag{4.1}$$

$$V_{\mathrm{T,REGP}} = V_{\mathrm{T,RE}} - \frac{\beta_{\mathrm{RE}}}{\beta_{\mathrm{GP}}}K_{\mathrm{in,GP}}, \tag{4.2}$$

$$\beta_{\mathrm{REGP}} = \frac{\beta_{\mathrm{RE}}}{\beta_{\mathrm{GP}}}. \tag{4.3}$$

where $C_{\mathrm{P}}(t)$ and $C_{\mathrm{T}}(t)$ are the tracer concentrations ($\mathrm{kBq \cdot mL^{-1}}$) at the post−injection time t (min) in arterial plasma and in the ROI or voxel spanning the target tissue, respectively; and $V_{\mathrm{T,RE}}$ and β_{RE}, (or $K_{\mathrm{in,GP}}$ and β_{GP}) are the estimates of the slope and intercept of the invasive RE (or the invasive GP plots) (see Equations (3.10) and (3.14) for their operational equations). Though Equation (4.1) has an equivalent form with Equation (3.4) of the Logan plot, the parameters $V_{\mathrm{T,REGP}}$ and β_{REGP} are estimated not by linear regression as in the

Logan plot but by the arithmetic operations on $V_{\mathrm{T,RE}}$, β_{RE}, $K_{\mathrm{in,GP}}$ and β_{GP} in Equations (4.2) and (4.3). Thus, the RE−GP method requires the measurement of the plasma input function to estimate these parameters of the invasive RE and GP plots.

The linearity period $t > t^*$ for the invasive RE−GP method mainly follows that of the invasive Logan plot (*31*). Thus, it is better to use the t^* suitable for the Logan plot in each application of the RE plot and the GP plot rather than to determine and use the individual t^* for the RE plot and the GP plot, which may be uncertain because of the slightly curved shape of the RE plot or high fluctuation in the GP plot as shown in Figure 3.1.

The RE−GP plot maintains the properties of the RE plot and GP plot such as computational efficiency and statistical characteristics. As the RE plot and the GP plot have the same independent variable in their model equation that is effectively noise−free, accuracies of their target parameter estimates and thus those of the RE−GP method are not affected by noisy $C_{\mathrm{T}}(t)$ in contrast to the Logan plot. However, the GP parameters are usually of high variance because of noisy $C_{\mathrm{T}}(t)$ in the dependent variable (Figure 3.2). Because of the division operations as well as the high−variance property of the GP plot, the direct application of Equations (4.2) and (4.3) to voxel TACs can lead to large spatial variations in the resulting images. Therefore, it is advantageous to apply a spatial smoothing filter to the GP parametric images before computing the parametric images of $V_{\mathrm{T,REGP}}$ and β_{REGP} (*31*).

The original RE–GP can circumvent not only the bias issue in the Logan plot but also that of the RE plot (Figure 3.2). As introduced in Section 4.1, the RE plot yields an underestimated V_{T} when sufficient time is not allowed for the tracer kinetics to reach the RE state (Figure 3.2). The missing information, which the RE plot failed to capture because of the violation of the RE requirement, can be compensated for by the results from the GP plot (Figure 3.2). In other words, the parameters obtained from the RE plot describe the components achieving the RE state during the PET scan, while those of the GP plot compensate for non–relative equilibrium (NRE) components inducing a bias in the RE parameters.

4.2.2 Noninvasive GA Approaches

As reviewed in Chapter 3, noninvasive GA approaches can be derived from their invasive counterparts by approximating the plasma input data ($\int_0^t C_{\mathrm{P}}(s)ds$) with a reference region input. For better readability, I recall the model equations for the Logan and GP plots:

$$\frac{\int_0^t C_{\mathrm{T}}(s)ds}{C_{\mathrm{T}}(t)} = DVR_{\mathrm{Logan}}\left(\frac{\int_0^t C_{\mathrm{R}}(s)ds + C_{\mathrm{R}}(t)/k_2'}{C_{\mathrm{T}}(t)}\right) + \beta_{\mathrm{Logan}}, \tag{4.4}$$

$$\frac{C_{\mathrm{T}}(t)}{C_{\mathrm{R}}(t)} = K_{\mathrm{in,GP}}^{\dagger}\frac{\int_0^t C_{\mathrm{R}}(s)ds}{C_{\mathrm{R}}(t)} + \beta_{\mathrm{GP}}^{\dagger}, \tag{4.5}$$

where $C_{\mathrm{R}}(t)$ is the time course of tracer concentration ($\mathrm{kBq \cdot mL^{-1}}$) in the reference region (usually ROI), and $k_2'(=-1/\beta_{\mathrm{Logan}}')$ is the apparent tissue–to–plasma efflux rate constant ($\mathrm{min^{-1}}$) in the

reference region when the reference data can be approximately described with 1TCM after t^* (see Section 3.2.1 for a more detailed description of k_2'; hereafter, I will refer to this linearity condition as 1TCM approximation for $t > t^*$). The slopes and the intercepts in these equations are associated with those of the invasive GA approaches in both tissue and reference regions as follows: $DVR_{\mathrm{Logan}} = V_{\mathrm{T,Logan}}/V'_{\mathrm{T,Logan}}$, $K^{\dagger}_{\mathrm{in,GP}} = K_{\mathrm{in,GP}}/V'_{\mathrm{T,Logan}}$, and $\beta^{\dagger}_{\mathrm{GP}} = K^{\dagger}_{\mathrm{in,GP}}/k_2' + \beta_{\mathrm{GP}}\, C_{\mathrm{P}}(t)/C_{\mathrm{R}}(t)$. Throughout the thesis, the superscript † indicates the parameters obtained from the noninvasive methods (except for DVR_{Method}).

Although the above two models were derived using the same approximation for the plasma integral (Equation (3.8)), the noninvasive RE plot (Equation (3.12)) was originally based on a different approximation (Equation (3.11)) (*69*). However, a slightly different model for the noninvasive RE plot can also be derived by using Equation (3.8):

$$\frac{\int_0^t C_{\mathrm{T}}(s)ds}{C_{\mathrm{R}}(t)} = DVR_{\mathrm{RE}}\frac{\int_0^t C_{\mathrm{R}}(s)ds}{C_{\mathrm{R}}(t)} + \beta^{\dagger}_{\mathrm{RE}}, \tag{4.6}$$

where $DVR_{\mathrm{RE}} = V_{\mathrm{T,RE}}/V'_{\mathrm{T,Logan}}$ and $\beta^{\dagger}_{\mathrm{RE}} = DVR_{\mathrm{RE}}/k_2' + \beta_{\mathrm{RE}}\, C_{\mathrm{P}}(t)/C_{\mathrm{R}}(t)$. It is noteworthy that when assuming the RE state of the reference region (hence, constant $C_{\mathrm{P}}(t)/C_{\mathrm{R}}(t)$), Equations (3.8) and (3.11) are equivalent and thus $\beta'_{\mathrm{RE}}C_{\mathrm{P}}(t)/C_{\mathrm{R}}(t) = -1/k_2' = \beta'_{\mathrm{Logan}}$; consequently, the above model (Equation (4.6)) is identical to the original one (Equations (3.12)).

The slopes and the intercepts of these noninvasive methods can be estimated by applying simple linear regression to data points after t^*. Depending on tracer kinetics, the Logan plot may require the use of individually pre-estimated k_2' or its population average, $\bar{k}_2'$.

4.2.3 Noninvasive RE-GP Plots

By substituting the plasma integral in Equation (4.1) with Equation (3.8) similarly as in the noninvasive Logan plot (Equation (3.9) or (4.4)), I newly derived the following relationships:

$$\frac{\int_0^t C_{\mathrm{T}}(s)ds}{C_{\mathrm{T}}(t)} = DVR_{\mathrm{REGP}}\left(\frac{\int_0^t C_{\mathrm{R}}(s)ds + C_{\mathrm{R}}(t)/k_2'}{C_{\mathrm{T}}(t)}\right) + \beta_{\mathrm{REGP}}, \tag{4.7}$$

$$DVR_{\mathrm{REGP}} = DVR_{\mathrm{RE}} - \frac{\beta_{\mathrm{RE}}}{\beta_{\mathrm{GP}}}K_{\mathrm{in,GP}}^{\dagger}. \tag{4.8}$$

Here, DVR_{RE} and $K_{\mathrm{in,GP}}^{\dagger}$ are the estimates of the slopes of the noninvasive RE and the noninvasive GP plots while β_{RE} and β_{GP} are those of the intercepts of the invasive approaches. Instead of individual calculations of β_{RE} and β_{GP}, their ratio $\beta_{\mathrm{RE}}/\beta_{\mathrm{GP}}$ can also be obtained using the intercept estimates ($\beta_{\mathrm{RE}}^{\dagger}$ and $\beta_{\mathrm{GP}}^{\dagger}$) from the two noninvasive methods as follows,

$$\frac{\beta_{\mathrm{RE}}}{\beta_{\mathrm{GP}}} = \beta_{\mathrm{REGP}} = \frac{\beta_{\mathrm{RE}}^{\dagger} - DVR_{\mathrm{RE}}/k_2'}{\beta_{\mathrm{GP}}^{\dagger} - K_{\mathrm{in,GP}}^{\dagger}/k_2'}. \tag{4.9}$$

Thus, given k_2', we are able to compute both the parameters corresponding to those of the noninvasive Logan plot by using the results from the noninvasive RE and the noninvasive GP plots.

Table 4.1. Parameters of two-tissue compartment model for a simulation study

Region	K_1	k_2	k_3	k_4	V_b	V_T
Striatum	0.37	0.04	0.09	0.0196	0.05	51.77
Cerebellum	0.48	0.05	0.02	0.0267	0.05	16.84

K_1 $(\mathrm{mL \cdot cm^{-3} min^{-1}})$: the rate constant for the delivery of the radioligand from arterial plasma to tissue; k_2 $(\mathrm{min^{-1}})$: the rate constant for the efflux from tissue; k_3 and k_4 $(\mathrm{min^{-1}})$: the rate constants for the binding and release from the neuroreceptor; V_b $(\mathrm{unitless})$: arterial blood volume fraction; and $V_T = (K_1/k_2)(1 + k_3/k_4)(\mathrm{mL \cdot cm^{-3}})$: total distribution volume.

4.2.4 Computer Simulations

I performed a simulation study to validate the noninvasive RE−GP method and evaluate its statistical properties. I generated 90−min noiseless tissue (striatum) and reference (cerebellum) TACs using reversible 2TCM parameters (Table 4.1) and a metabolite−corrected plasma input function for [^{18}F]FP−CIT (*74*). Then, we simulated noisy TACs by adding Gaussian noise with zero mean and Poisson−like variance, as modeled in previous studies (*22, 29, 87, 88*), to the non−decay−corrected TAC of the tissue at each of 4 different noise levels α $(= 0.2, 0.4, 0.6,$ and $0.8)$. The noise levels of real ROI and voxel data correspond to $\alpha \leq 0.2$ and $0.2 < \alpha \leq 0.6$, respectively.

For each α, I analyzed a total of 1,000 realizations of noisy TAC using the noninvasive RE, GP, and Logan plots, and the simplified reference tissue model (SRTM) (*36*). Because of large CVs at high noise levels of the SRTM even after removing outliers, we also applied its reduced model with fixing k_2' as a pre−estimated one (SRTM2)(*89*). For all the GA methods, I used $t^* = 60$ min. Then, I computed the parameters of the proposed RE−GP method by applying Equations (4.8) and (4.9) to those of the RE and GP methods; moreover, I used the mean of the GP parameters instead of applying a spatial smoothing filter to reduce their high variances (see Section 4.2.1).

In addition, I examined the effects of different k_2' values on the proposed and Logan methods: 1) one $(k_2' = 0.0200)$ was computed from

the simulation parameters by the 1TCM approximation for $t > t^*$ (*29, 60*) (see Section 3.2.1 and Equation (3.6)), 2) another ($k_2' = 0.0303$) was obtained by applying the SRTM to the noiseless TACs, and 3) the infinite value corresponded to ignoring the k_2' term.

For each set of the 1,000 resulting DVR estimates, we measured bias and coefficient of variation (CV) as in our previous study (*22*) after removing outliers; the ground truth ($DVR = V_T/V_T' = 3.0743$) was computed using the simulation parameters (Table 4.1), and outliers were defined by physiologically extreme values that are smaller than 1 or larger than 15 as in (*74*).

4.2.5 Human [^{18}F]FP-CIT PET Data

To assess the applicability to real data, I used dynamic [^{18}F]FP-CIT human brain PET data from nineteen Parkinson's disease (PD) patients (mean age, 56.6 ± 7.1 years; age range, 42–69 years) and nine age-matched healthy volunteers (mean age, 56.0 ± 7.0 years; age range, 45–65 years), which were selected from our previous study (*16*). A detailed description of the characteristics of the participants and image acquisition can be found in the previous study. In brief, after an intravenous bolus injection of 185 MBq (5.0 mCi) [^{18}F]FP-CIT, each participant underwent a 90-minute dynamic scan (Siemens Biograph 40 Truepoint PET/CT, Knoxville, TN, USA). The PET data were acquired in three-dimensional list mode and then rebinned into 50 time

frames (8 × 15, 16 × 30, 10 × 60, 10 × 240, and 6 × 300 s). Dynamic PET images were subsequently reconstructed by filtered back projection with routine corrections for physical effects; each reconstructed image had a dimension of 256 × 256 × 148 and a voxel size of 1.3364 × 1.3364 × 1.5 mm^3.

For putamen, caudate nucleus, globus pallidus, amygdala, and cerebellum, regional average TACs were extracted from the dynamic images by applying MRI-based ROI masks (see (*16*) for details of processing). I analyzed each ROI TAC using the proposed method, the noninvasive Logan plot, and the SRTM with the cerebellum for the reference region. For the RE-GP and Logan methods, I used $t^* = 60$ and the k_2' values obtained by the SRTM. Then, I assessed agreements of the ROI DVR estimates between each GA method and the SRTM. I explored the effect of neglecting k_2' terms on the two GA methods as well.

DVR parametric images were generated by applying the proposed method and the noninvasive Logan plot to voxel TACs on the reconstructed dynamic images. As in (*31*) (see Section 4.2.1), to reduce the variability of GP parameters, I applied a two-dimensional spatial smoothing on each transverse slice of the $K_{\mathrm{in,GP}}^{\dagger}$ image with equal weighting for 10×10 pixels and on the $(\beta_{\mathrm{GP}}^{\dagger} - K_{\mathrm{in,GP}}^{\dagger}/k_2')$ image with a larger window of 30×30 pixels. Finally, the ROI-mean values of DVR images were compared with the corresponding ROI results to investigate the effects of high-level noise on each method.

4.3 Results

4.3.1 Regional Time–activity Curves and Graphical Plots

Figure 4.1 shows representative simulated TACs and *in vivo* population–averaged ROI TACs of [^{18}F]FP–CIT, and the corresponding tissue–to–reference ratios. For all the ROIs except for the cerebellum, the curves showed early rapid increase and subsequent slow clearance as in previous studies (*11, 74*); as a result, the tissue–to–reference ratios increased with time, indicating that the corresponding kinetics were not in the RE state until 90 min after injection.

For both the simulated and real ROI data, the RE plot, the GP plot, and the Logan plot (for all the considered k_2' values) attained approximately linearity after $t^* = 60$ min post–injection (corresponding to the last 6 time points) as illustrated in Figure 4.2. The GP plot showed positive slopes owing to the NRE kinetics. In the meantime, the RE plot demonstrated the lowest slopes while the Logan plot yielded larger and k_2'–dependent slopes, implying the NRE–induced bias in the DVR_{RE} and, furthermore, the NRE–induced and k_2'–dependent bias in the DVR_{Logan}.

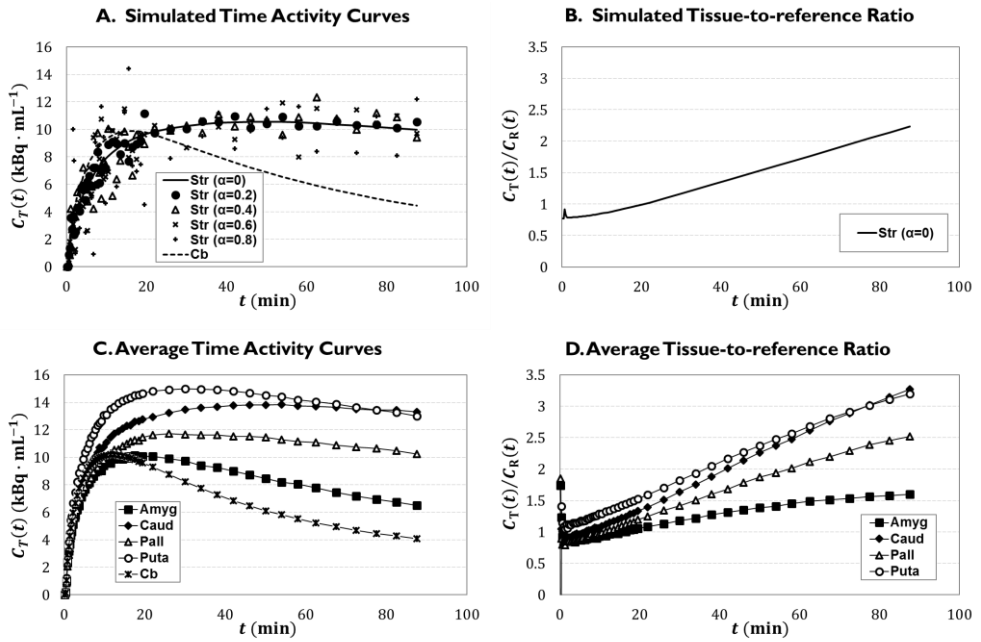

Figure 4.1. Kinetics of [^{18}F]FP-CIT. (A) Simulated time-activity curves (TACs) over a range of noise levels (α) for tissue (striatum, Str) and a noiseless one for reference (cerebellum, Cb). (B) The ratio of noiseless tissue TAC to reference TAC. (C) Region-of-interest TACs in amygdala (Amyg), caudate (Caud), globus pallidus (Pall), and putamen (Put) averaged over 28 participants from [^{18}F]FP-CIT PET in the human brain. (D) The corresponding ratio of tissue-to-reference activities from the human data.

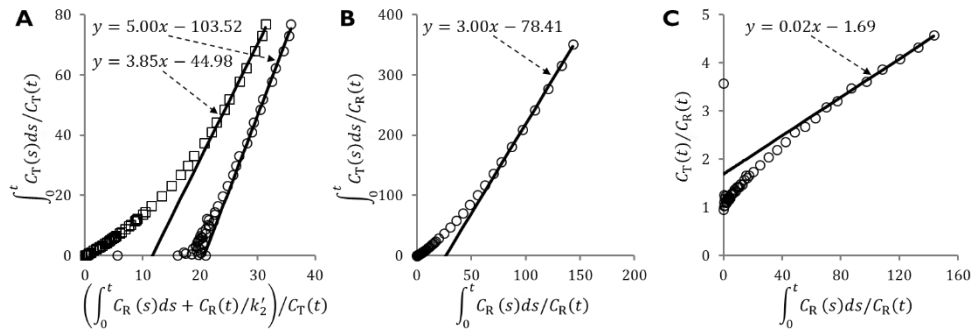

Figure 4.2. Typical graphical plots for the measured regional time–activity curves from the [^{18}F]FP–CIT PET studies: (A) Logan plot with k_2' (circle) and Logan plot without k_2' (square), (B) Relative equilibrium (RE) plot, and (C) Gjedde–Patlak (GP) plot.

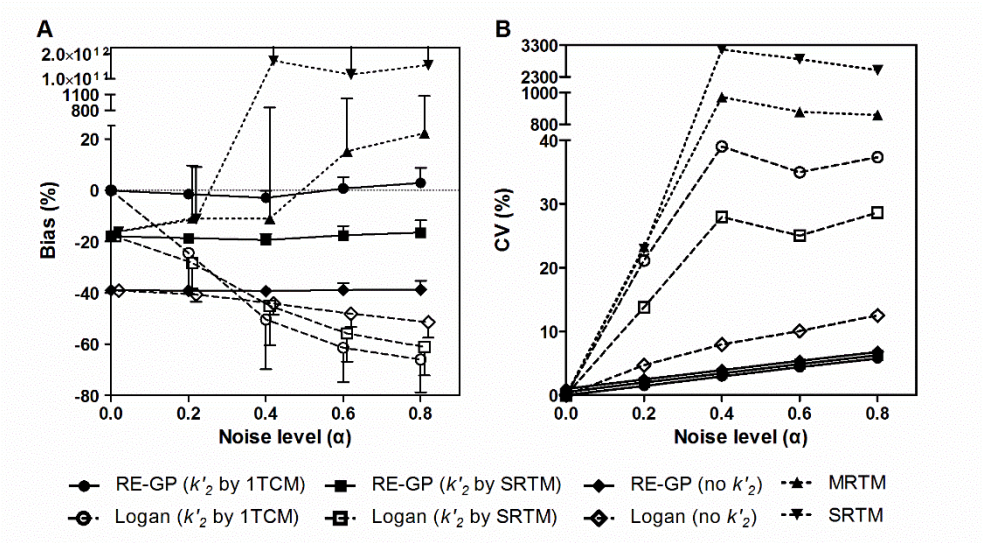

Figure 4.3. Bias (A) and coefficient of variation, CV, (B) of ***DVR*** estimated with various methods for simulated [^{18}F]FP-CIT time-activity curves with different noise levels ($\boldsymbol{\alpha}$). Error bars in (A) represent the standard deviation in the bias. For $\boldsymbol{k'_2}$, we used $\mathbf{0.0200}$ (obtained by 1TCM approximation for $t > t^*$), $\mathbf{0.0303}$ (by the SRTM), and infinity (no $\boldsymbol{k'_2}$ term). To allow a better visualization, graphs in (A) except for those of the Logan with $\boldsymbol{k'_2}$ by 1TCM and the RE-GP were slightly shifted to the right. Graphs of the RE-GP with $\boldsymbol{k'_2}$ by SRTM or with no $\boldsymbol{k'_2}$ in (B) were also shifted upward although the three graphs of RE-GP in (B) exactly overlap each other.

Table 4.2. Percentages of outliers in the simulation results using various methods

Methods	Number of outliers (%)			
	$\alpha = 0.2$	0.4	0.6	0.8
RE−GP (k_2' by 1TCM)	0	0	0	0
Logan (k_2' by 1TCM)	0.5	11.5	29.1	41
RE−GP (k_2' by SRTM)	0	0	0	0
Logan (k_2' by SRTM)	0	2.8	12.3	24
RE−GP (no k_2')	0	0	0	0
Logan (no k_2')	0	0	0.2	1
SRTM	0	5.6	14	19.4
SRTM2 (k_2' by SRTM)	0	0	0	0

4.3.2 Simulation Results

For noiseless data ($\alpha = 0$), the noninvasive RE−GP and Logan plots produced similar DVR estimates independent of k_2' while their accuracies were dependent on the k_2' values as shown in Figure 4.3A. Computing k_2' by the 1TCM approximation for $t > t^*$, the two methods produced almost unbiased results. However, the use of k_2' estimated by the SRTM led to biased results, which were similar to those from the SRTM or the SRTM2. When ignoring the k_2' term, the largest biases were observed in both the RE−GP and Logan methods.

Although there was no discrepancy between the noninvasive RE−GP and Logan plots for noiseless data ($\alpha = 0$), the discrepancy increased with increasing noise level owing to noise−induced bias in the Logan plot (Figure 4.3A). Furthermore, the discrepancy increased as the k_2' values decreased (from infinity to 0.0200) because the noise−induced biases in the Logan plot were dependent on k_2'. Conversely, the accuracy of DVR_{REGP} was almost independent of noise levels.

The results of the RE−GP and the SRTM2 with the k_2' by the SRTM showed similar levels of bias consistently at all noise levels without introducing outliers (Figure 4.3A; see Table 4.2 for the number of outliers in each method). However, the underestimation of the SRTM declined along with higher noise levels at the expense of considerable increases of CVs even after excluding extreme outliers, showing growing deviations from those of the RE−GP and the SRTM2.

As shown in Figure 4.3B, the SRTM demonstrated the highest CV values among the methods. The CVs of the SRTM2 was reduced considerably compared to the SRTM but they were still larger than those of the RE−GP based on the same k_2' value. Meanwhile, the CVs of the RE−GP results were lowest, most stable over a range of noise levels, and independent of k_2' whereas those from the Logan plot were intermediate, slightly increased with higher noise levels, and rapidly decreased with larger k_2'.

4.3.3 Application to Human Data

In common with the simulation, because of the NRE effects, ROI DVR estimates from the RE, the Logan, and the RE−GP methods when neglecting k_2' were severely lower compared with those from the SRTM as illustrated in Figure 4.4; Nonetheless, they showed high correlations with the SRTM ($r \geq 0.90$). Conversely, when using the k_2' obtained by the SRTM, the results from the Logan and RE−GP methods demonstrated good agreements with the SRTM results (Figure 4.4D and Figure 4.4E). Regardless of whether k_2' was used, the RE−GP method provided very similar DVR values to the Logan plot, as shown in Figure 4.5.

In voxel−wise quantification, the RE−GP with k_2' (by the SRTM) produced parametric images with good quality (Figure 4.6B) and ROI−mean values similar to the corresponding results of ROI analysis

(Figure 4.7B). However, ignoring k'_2 decreased the image intensity while maintaining the image quality (Figure 4.6D and Figure 4.7D). Meanwhile, the DVR images from the Logan plot showed lower image intensity and poorer quality than those from the RE−GP as illustrated in Figure 4.6A and Figure 4.6C. The Logan plot with k'_2 suffered from noticeable noise−induced bias (Figure 4.7A) unlike the RE−GP with k'_2. Conversely, despite the NRE induced bias, the ROI−mean values of DVR images from the Logan plot when neglecting k'_2 were less sensitive to high−level noise in each voxel than when using k'_2, showing a good consistency with the corresponding ROI results (Figure 4.7). However, the image quality of the Logan plot without k'_2 was still inferior to that of the RE−GP without k'_2.

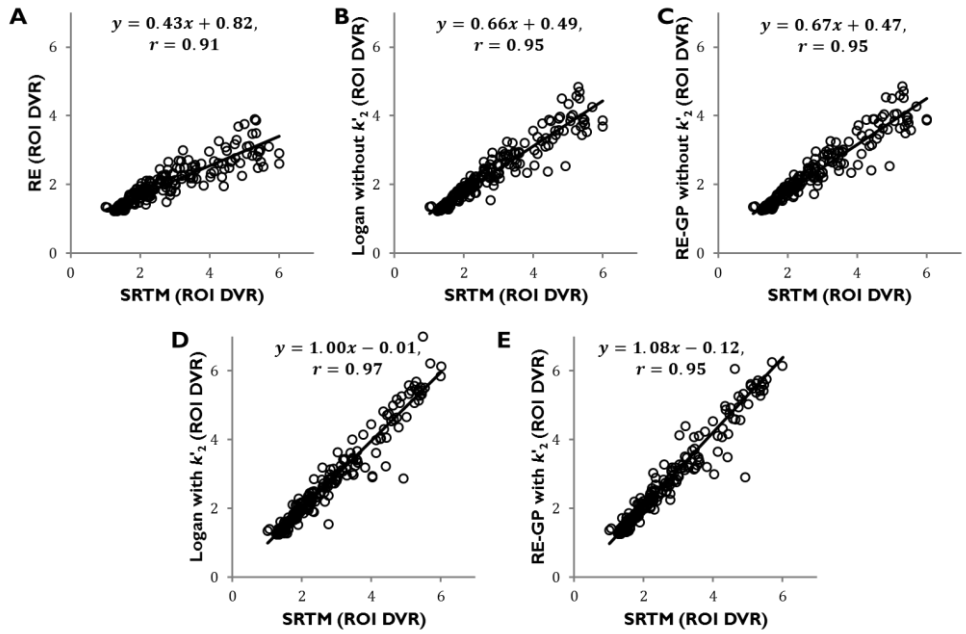

Figure 4.4. Linear relationship between regional ***DVR*** estimates from each noninvasive graphical analysis and those from the simple reference tissue model (SRTM). (A) RE; (B) Logan without $\boldsymbol{k_2'}$; (C) RE−GP without $\boldsymbol{k_2'}$; (D) Logan with $\boldsymbol{k_2'}$; and (E) RE−GP with $\boldsymbol{k_2'}$. For $\boldsymbol{k_2'}$, we used the values pre−estimated by the SRTM.

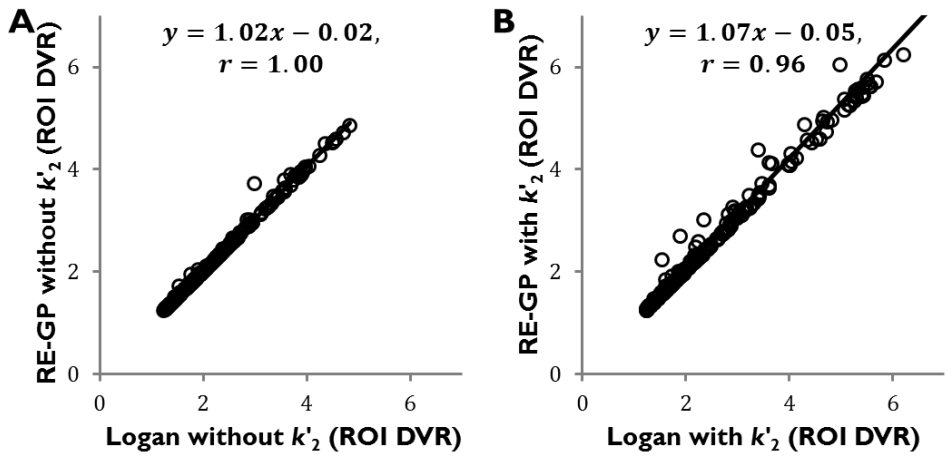

Figure 4.5. Agreement of regional $\boldsymbol{DVR}$ between the proposed and the noninvasive Logan methods when (A) neglecting $\boldsymbol{k_2'}$ and (B) using it.

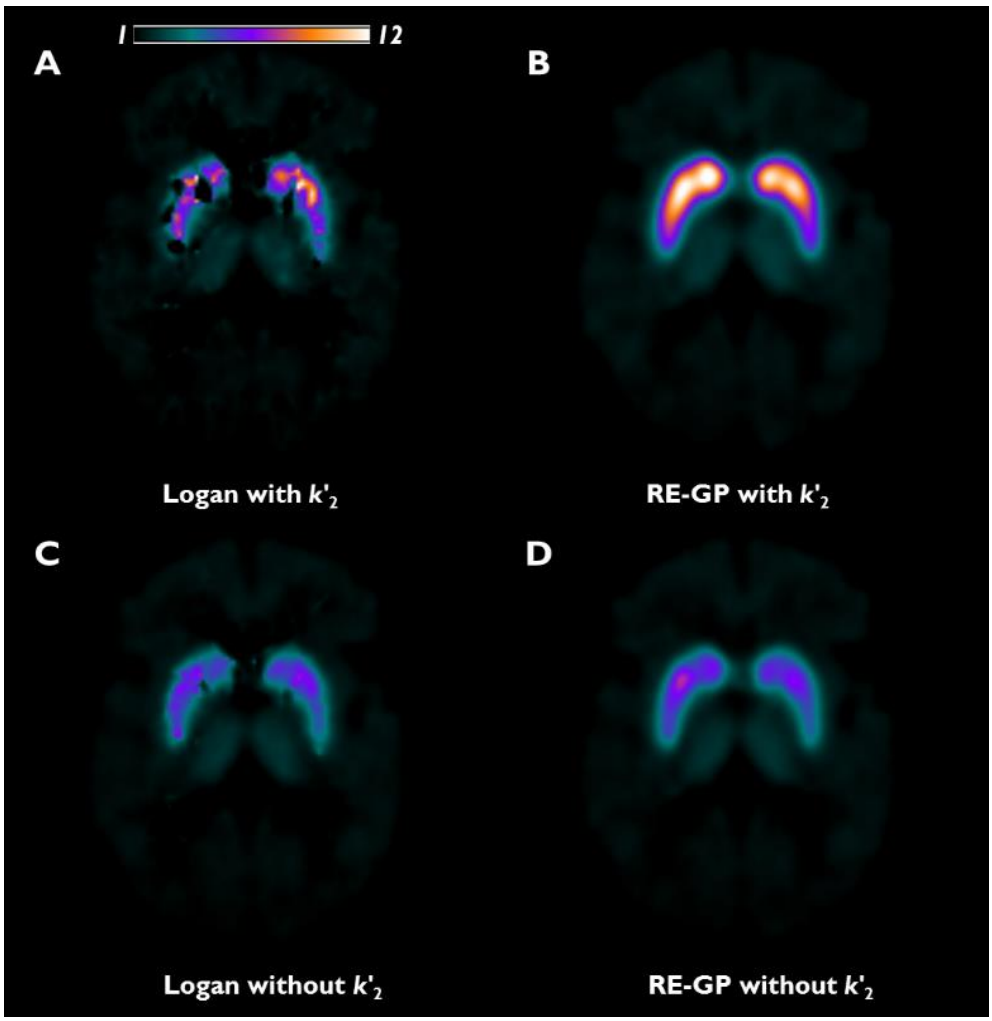

Figure 4.6. Transverse planes of representative parametric images of $\boldsymbol{DVR}$ generated by (A) Logan with $\boldsymbol{k'_2}$; (B) RE-GP with $\boldsymbol{k'_2}$; (C) Logan without $\boldsymbol{k'_2}$; and (D) RE-GP without $\boldsymbol{k'_2}$. For $\boldsymbol{k'_2}$, we used the values pre-estimated by the SRTM.

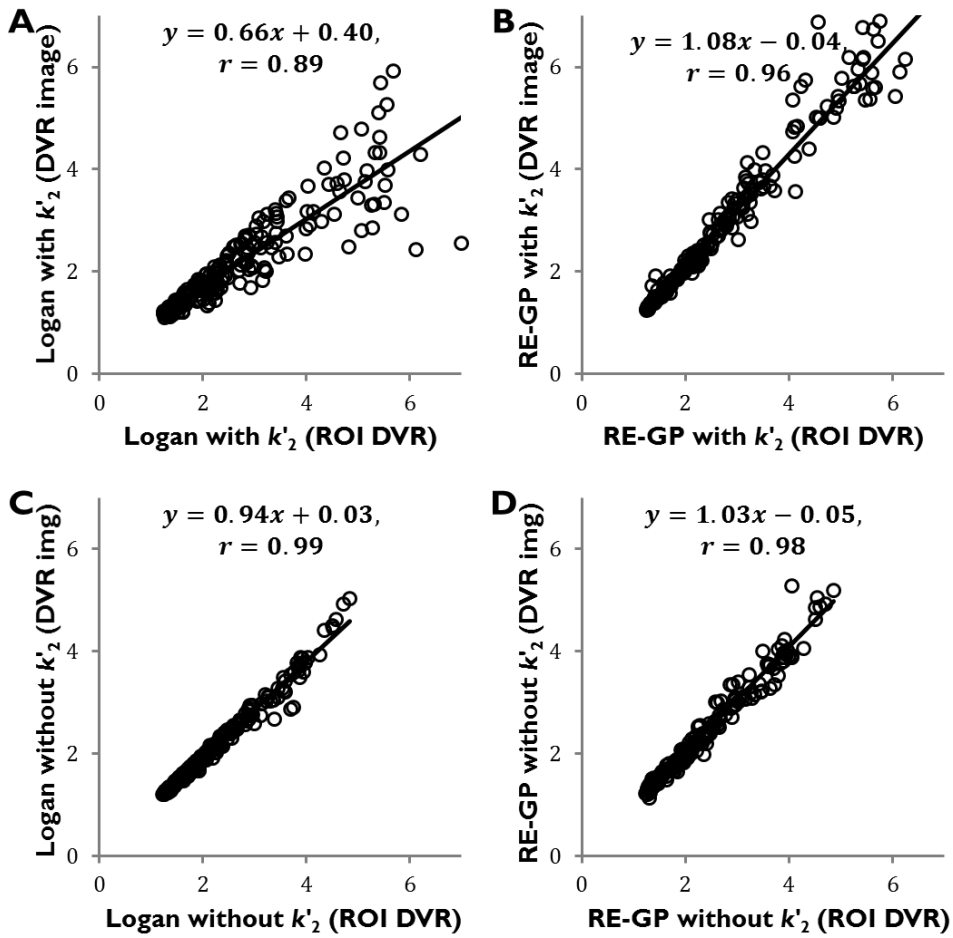

Figure 4.7. Linear relationship between ROI-mean values of $\boldsymbol{DVR}$ parametric images and the corresponding estimates in ROI analysis for various graphical analysis methods: (A) Logan with $\boldsymbol{k'_2}$; (B) RE-GP with $\boldsymbol{k'_2}$; (C) Logan without $\boldsymbol{k'_2}$; and (D) RE-GP without $\boldsymbol{k'_2}$. Each panel corresponds to the $\boldsymbol{DVR}$ image in Figure 4.6.

4.4 Discussion

In this chapter, I presented a new bi-graphical method based on reference region data and the noninvasive RE and GP plots. I investigated its validity and statistical properties with a simulation study and then evaluated its feasibility for the quantification of [^{18}F]FP-CIT PET in the human brain. The results revealed that the arithmetic combination of the RE and GP parameters yields DVR estimates in agreement with the noninvasive Logan plot for noise-free simulated and clinical ROI data by correcting the NRE-induced bias, and that k_2' determines their accuracies or the amount of bias correction. The k_2' computed by 1TCM approximation turned out to be the optimal choice, which led to almost unbiased results. The use of k_2' from the SRTM led to biased results, but they showed good agreement with those from the SRTM, implying that estimating k_2' from the SRTM would be a promising practical approach when no arterial input is given. Furthermore, unlike the Logan plot whose accuracy and variability depended on both the noise levels and the k_2' values, the proposed RE-GP approach showed the accuracy almost independent of the noise levels, and the variability independent of k_2' and relatively stable over the noise levels. These favorable statistical properties made the proposed method outperform the Logan plot in the parametric image generation using *in vivo* data.

4.4.1 Characteristics of [^{18}F]FP-CIT PET Data

The [^{18}F]FP-CIT is a very promising radioligand for dopamine transporter (DAT) imaging because of high affinity and selectivity for the DAT and relatively faster kinetics than other DAT-imaging tracers (*11, 74, 90, 91*). Nevertheless, its slow kinetics in striatum required a dynamic PET scan of more than 90-min duration for the reliable quantification of its specific binding to the DAT through a kinetic analysis (*74*) and yielded NRE components in 90-min data as illustrated in Figure 4.1B and Figure 4.1D. Moreover, its rapid metabolism might hamper the accurate measurement of plasma input function for such long scan duration (*11*), thereby demanding the use of reference-region-based approaches for the quantification. These characteristics of [^{18}F]FP-CIT present the rationale for a noninvasive method capable of enduring the slow kinetics, such as the proposed RE-GP method.

4.4.2 Kinetic Methods for [^{18}F]FP-CIT PET

The [^{18}F]FP-CIT PET has been used via a ratio analysis for studying various kinds of Parkinsonism (*92-99*). However, kinetic methods to quantify the specific bindings of [^{18}F]FP-CIT have been evaluated in a very limited number of studies, mostly by ROI analysis. In (*11*), the regional brain uptake of [^{18}F]FP-CIT was evaluated using both the invasive and noninvasive Logan methods (using the population average

of k_2' estimated by the invasive Logan plot). Although a good agreement was found between the two methods, they were not compared with any compartmental model, but were compared only with a ratio method. In (*74*), the SRTM provided a negatively biased but noise-robust estimation of binding potential for 90-min striatal ROI data. Conversely, the plasma-input compartment models suffered from large numbers of outliers because of the unclear preference between reversible and irreversible model structures (or very small k_4).

4.4.3 Correction for NRE Effects

The aforementioned unclear model preference is likely based on the NRE components because their slow kinetics could be considered as approximately irreversible within a limited scan duration (*31*). Based on this premise, the invasive RE-GP method employs the invasive GP plot to capture the V_T information from the apparently irreversible components that could be hardly quantified using the invasive RE plot. Similarly, the noninvasive RE-GP method takes advantage of the noninvasive RE and GP methods to describe the RE components and the NRE components of DVR, respectively. As described in Section 4.3.1 and Figure 4.2, the NRE state might affect not only the results from the RE plot but also those from the Logan and RE-GP approaches without k_2'. Thus, the proposed RE-GP method requires k_2' as well as the GP plot to correct for the NRE effects.

4.4.4 Linearity Condition

Fundamentally, the noninvasive RE−GP method provides the indirect implementation of the noninvasive Logan plot. Therefore, the two methods share not only the k_2'−dependent correction of NRE effects but also the linearity condition. As stated in section 4.2.1, the validity of V_T estimates from the invasive RE−GP method relies on the linearity condition of the invasive Logan plot, which requires the tracer kinetics in tissue to follow 1TCM after t^* and can usually be achieved earlier than the RE condition (*30, 31, 100*). Theoretically, the noninvasive Logan and RE−GP methods should follow that linearity condition as well since it is invariant during the derivations of the two methods. Therefore, even if the apparently irreversible components achieve asymptotic linearity in the noninvasive GP plot, a violation to the Logan linearity condition may lead to biased DVR estimates. In practice, error in the pre−estimated k_2' may change the linearity condition as illustrated in Figure 4.2A. In this study, the Logan linearity condition was achieved after $t^* = 60$ min for all the used k_2' values.

4.4.5 Advantages over the Noninvasive Logan plot

The indirect implementation gives the RE−GP method two advantages over the Logan plot: favorable statistical properties and computational efficiency. These are particularly useful for parametric image

generation, which is challenging because of the huge numbers of voxels and the high-level noise therein (*4, 8, 18, 19, 22, 30*).

The statistical properties of the RE-GP approach are determined by those of the RE and GP methods. The parameters of the RE and GP methods can be estimated without noise-induced bias since the two methods share almost noiseless independent variable (Equations (4.5) and (4.6)) in contrast to the Logan plot. In addition, the results of the GP plot usually have higher variability than those of the RE plot because the numerator ($C_T(t)$) in its dependent variables has higher noise levels than that ($\int_0^t C_T(s)ds$) of the RE plot. Moreover, the results from the GP plot are incorporated in the denominator for the computation of the RE-GP parameters. Consequently, noise in data seems to dominantly affect the variability of the results from the RE-GP rather than the accuracy.

The above hypothesis is supported by our results that the k_2'-dependent accuracies of the RE-GP results were independent of the noise levels. The quality of the parametric images further implies that the use of smoothing or mean filters for the GP parameters can improve the variability property. Conversely, because of noise-induced bias, k_2'-dependent accuracies of the Logan plot increasingly deteriorated as the noise level rose. Furthermore, the noise-induced biases were more severe for smaller k_2' (for the range of k_2' considered); this is because smaller k_2' yields larger (or less underestimated) DVR as demonstrated in our results for noiseless data, and the extent of the bias depends on the magnitude of the parameters as well as on the

noise level (*79*).

Meanwhile, the independent variable shared by the RE and GP methods may offer the computational advantage to the RE–GP method, too (*31, 69, 100*). Because the independent variable consists of only reference region data, it is applied commonly to all voxels or ROIs, requiring only one matrix conversion for the whole analysis, e.g. the generation of one parametric image. Besides, this common independent variable enables reconstructing parametric images of the RE or GP plot directly from raw projection data (*20, 101, 102*). Conversely, even though the Logan plot requires fairly simple computation compared to nonlinear approaches, a nonlinear involvement of tissue activity data in the independent variable of the Logan plot requires a matrix computation for every voxel, and makes direct reconstruction more difficult (*20*). Furthermore, the noise in the tissue data may cause unstable matrix conversion at the voxel levels (*100*).

4.4.6 Comparison with the SRTM

In the *in vivo* quantifications, I compared the ROI results from both the RE–GP and Logan methods to those from the SRTM because of SRTM's reliability as shown in (*74*). Their results demonstrated good agreements when k_2' was estimated using the SRTM; additionally, even when the k_2' term was ignored, they showed good correlations despite the NRE–induced bias.

I observed a similar trend of good agreement in the low-noise simulation. In keeping with the previous study (*74*), however, the results from the SRTM and the SRTM2 showed negative biases for the simulated data without noise, compared with the simulated value of DVR $(=V_T/V'_T = 3.0743)$. Conversely, given the accurate estimate of k_2' (by 1TCM approximation), both the Logan and RE-GP methods led to almost unbiased results.

Considering the model independence of the GA approaches, these results imply that the biases in the SRTM and the SRTM2 were based on the conflict between their 1TCM assumptions for tissue and reference regions and the data simulated using 2TCMs. Hence, I claim that the proposed method outperforms the SRTM or the SRTM2 if k_2' can be accurately pre-estimated (for example, by the invasive Logan) or outperforms at least at high noise levels if k_2' is given by the SRTM. Moreover, irrespective of k_2', it outperforms the Logan plot at high noise levels.

4.4.7 Simulation Settings

It may seem that there is a discrepancy between the simulation results in this study and in (*74*) because simulation settings are slightly different from each other.

First, the range of noise levels considered were different. In (*74*), simulations were performed only at low noise levels seen in clinical

practice: 2.5 and 5% in terms of average CV over the last 60% of the frames (i.e. for the curve >5 min) (also refer to (*103*) for the definition of noise level). However, in this study, I included a broader range of noise levels $(0.2 \leq \alpha \leq 0.8)$, and the levels considered in (*74*) correspond to $\alpha \leq 0.2$ level (≤ about 7% CV), which is similar with those of our real ROI data. In these low noise levels, the SRTM results of the two studies contained no outliers.

Second, the definition of bias and the ground truth for its computation are not same. In (*74*), the accuracy was determined as the ratio of the estimated BP value over simulated BP value. The simulated BP value was computed as $BP_{\mathrm{2T-4k}}^{\mathrm{str}} - BP_{\mathrm{2T-4k}}^{\mathrm{Cb}} = \frac{k_3^{\mathrm{str}}}{k_4^{\mathrm{str}}} - \frac{k_3^{\mathrm{cb}}}{k_4^{\mathrm{cb}}} = \frac{0.09}{0.0196} - \frac{0.02}{0.0267} \approx 3.85$ under the assumption that there are components of not only specific binding but also slow nonspecific binding; $BP_{\mathrm{2T-4k}} = \frac{k_3}{k_4}$ is the binding potential estimated from 2TCM with 4 parameters. In addition, the average accuracy of BP values estimated by SRTM was 0.4 ± 0.1 in the simulation, which corresponds to $DVR = BP + 1 = 0.4 \times 3.85 + 1 = 2.54$. However, I used $DVR = V_{\mathrm{T}}/V_{\mathrm{T}}' = 3.0743$ as the ground truth, and observed about $\leq 20\%$ bias in the SRTM results at $\alpha \leq 0.2$ level, which corresponds to $DVR = 2.46$.

In sum, when accounting for the differences in simulation setting, the results of the SRTM are very similar between the two studies.

4.4.8 Noninvasiveness

Because of k_2' -dependancy, a noninvasive method for accurate estimation of k_2' is imperative for the practical use (without blood sampling) of the proposed method. So far, however, there is no existing approach to obtain unbiased k_2' estimates without plasma input function; it is possible only through applying the invasive Logan plot to the reference TAC or estimating individual rate constants of 2TCM. Therefore, in a strict sense, the proposed method and also the noninvasive Logan plot cannot be considered as a noninvasive method without a use of $\bar{k}_2'$ or any preliminary one obtained by noninvasive ways.

In this study, the use of $\bar{k}_2'$ was not evaluated because, based on best knowledge, there is no credible population average of k_2' of cerebellum available now. Although Kazumata et al. (11) reported population averages of K_1 and V_T in cerebellum, their ratio cannot be necessarily accurate estimate of $\bar{k}_2'$, only providing its approximate at best. Furthermore, the main points of this study are 1) that the NRE-induced bias in the noninvasive RE plot can be reduced and the noninvasive Logan plot can be implemented by using the parameter estimates from the noninvasive GP plot together with k_2' estimates (obtained somehow), 2) that the accuracy of k_2' determines the amount of reduction in the NRE-induced bias and equally affects the results from the noninvasive Logan plot and the proposed RE-GP method for

noiseless data, and 3) that the different results at high noise levels between the two methods are mainly due to noise-induced bias in the Logan plot. All these things are well supported by the current simulation results. In this context, I don't expect that an additional simulation with other population average value will provide much more information. In other words, whether the population average is close to the true k_2' or not, the two methods will perform equally at low noise levels; the RE-GP will outperform the Logan plot at high noise levels; and the RE-GP will offer any amount of reduction in the NRE-induced bias, which is consistent and reliable for all noise levels.

Instead, I considered the use of k_2' estimated by SRTM from ROI data as a reasonable practical approach. In the application to human data, the use of k_2' by SRTM made the proposed method to produce $DVRs$ that were highly correlated with those of SRTM although the inaccuracy of k_2' led to negative bias in the ROI results of the two methods, to a similar extent. Similar trends were observed in the simulation at low noise levels; furthermore, the RE-GP method provided consistent accuracies with the lowest CVs for all the considered noise levels while even the SRTM2 showed larger CVs than the RE-GP at high noise levels. In sum, even if using the k_2' by SRTM, which is biased, the RE-GP will perform as well or better than the SRTM.

Chapter 5 Summary and Conclusion

In this thesis, I have presented a novel noninvasive GA-based parametric image generation from dynamic neuroreceptor PET data, with an overview of GA-based approaches. The proposed noninvasive RE-GP approach provides DVR estimation comparable to the noninvasive Logan graphical analysis for noise-free simulated and clinical ROI data. In common with its invasive counterpart, the proposed RE-GP can reduce a noise-induced bias of the Logan method at high noise levels. Contrary to the invasive RE-GP approach, which can almost reduce the NRE-induced bias, this approach yields partial to full reduction of the NRE-induced bias, depending on k_2' value. Furthermore, it is free from issues related to arterial blood sampling if a pre-estimated k_2' is given. Therefore, despite k_2' -dependent accuracy, this approach might be useful in parametric image generation for slow kinetic tracers that require a long-lasting PET scan.

Bibliography

1. Ichise M, Meyer JH, Yonekura Y. An introduction to PET and SPECT neuroreceptor quantification models*. *J Nucl Med.* May 1, 2001 2001;42(5):755–763.

2. Meyer JH, Ichise M. Modeling of receptor ligand data in PET and SPECT imaging: A review of major approaches. *J Neuroimaging.* 2001;11(1):30–39.

3. Watabe H, Ikoma Y, Kimura Y, Naganawa M, Shidahara M. PET kinetic analysis—compartmental model. *Ann Nucl Med.* 2006;20(9):583–588.

4. Zaidi H, Shidahara M. Neuroreceptor imaging. In: Choi I-Y, Gruetter R, eds. *Neural metabolism in vivo*: Springer; 2012:305–329.

5. Lee JS, Lee DS. Tracer kinetic analysis for PET and SPECT. In: Farncombe T, Iniewski K, eds. *Medical imaging: Technology and applications*: CRC press; 2013.

6. Mintun MA, Raichle ME, Kilbourn MR, Wooten GF, Welch MJ. A quantitative model for the in vivo assessment of drug binding

sites with positron emission tomography. *Ann Neurol.* 1984;15(3):217–227.

7. Carson RE. Tracer kinetic modeling in PET. In: Bailey DL, Townsend DW, Valk PE, Maisey MN, eds. *Positron emission tomography*. London: Springer; 2005:127–159.

8. Feng DD. *Biomedical information technology*: Academic Press; 2008.

9. Cherry SR, Sorenson JA, Phelps ME. *Physics in nuclear medicine*: Elsevier Health Sciences; 2012.

10. Koeppe R, Holthoff V, Frey K, Kilbourn M, Kuhl D. Compartmental analysis of [^{11}C]flumazenil kinetics for the estimation of ligand transport rate and receptor distribution using positron emission tomography. *J Cereb Blood Flow Metab.* 1991;11(5):735–744.

11. Kazumata K, Dhawan V, Chaly T, et al. Dopamine transporter imaging with Fluorine-18-FPCIT and PET. *J Nucl Med.* September 1, 1998 1998;39(9):1521–1530.

12. Chen M-K, Lee J-S, McGlothan JL, et al. Acute manganese administration alters dopamine transporter levels in the non-human primate striatum. *Neurotoxicology.* 2006;27(2):229-236.

13. Lim K, Kwon J, Jang I, et al. Modeling of brain D_2 receptor occupancy-plasma concentration relationships with a novel antipsychotic, YKP1358, using serial PET scans in healthy volunteers. *Clin Pharmacol Ther.* 2007;81(2):252-258.

14. Weerts EM, Kim YK, Wand GS, et al. Differences in δ-and μ-opioid receptor blockade measured by positron emission tomography in naltrexone-treated recently abstinent alcohol-dependent subjects. *Neuropsychopharmacol.* 2008;33(3):653-665.

15. Kim JW, Lee JS, Kim SJ, et al. Compartmental modeling and simplified quantification of [^{11}C]sertraline distribution in human brain. *Arch Pharm Res.* 2012;35(9):1591-1597.

16. Lee J-Y, Seo SH, Kim YK, et al. Extrastriatal dopaminergic changes in Parkinson's disease patients with impulse control disorders. *J Neurol Neurosurg Psychiatry.* January 1, 2014 2014;85(1):23-30.

17. Carson RE. Tracer kinetic parametric imaging in PET. Paper presented at: Biomedical Imaging: Nano to Macro, 2004. IEEE International Symposium on, 2004.

18. Lee JS, Lee DS, Ahn JY, et al. Generation of parametric image of regional myocardial blood flow using $H_2{}^{15}O$ dynamic PET and a linear least-squares method. *J Nucl Med.* 2005;46(10):1687–1695.

19. Cselényi Z, Olsson H, Halldin C, Gulyás B, Farde L. A comparison of recent parametric neuroreceptor mapping approaches based on measurements with the high affinity PET radioligands [^{11}C]FLB 457 and [^{11}C]WAY 100635. *NeuroImage.* 10/1/2006;32(4):1690–1708.

20. Wang G, Qi J. Direct estimation of kinetic parametric images for dynamic PET. *Theranostics.* 2013;3(10):802–815.

21. Gunn RN, Lammertsma AA, Hume SP, Cunningham VJ. Parametric imaging of ligand-receptor binding in PET using a simplified reference region model. *NeuroImage.* 1997;6(4):279–287.

22. Kim SJ, Lee JS, Kim YK, et al. Multiple linear analysis methods for the quantification of irreversibly binding radiotracers. *J Cereb Blood Flow Metab.* 2008;28(12):1965–1977.

23. Bentourkia Mh, Zaidi H. Tracer kinetic modeling in PET. *PET Clinics.* 2007;2(2):267–277.

24. Wienhard K, Schmand M, Casey ME, et al. The ECAT HRRT: Performance and first clinical application of the new high resolution research tomograph. *IEEE Trans Nucl Sci.* 2002;49(1):104–110.

25. Zhou Y, Huang S-C, Bergsneider M, Wong DF. Improved parametric image generation using spatial-temporal analysis of dynamic PET studies. *NeuroImage.* 2002;15(3):697–707.

26. Alpert NM, Yuan F. A general method of Bayesian estimation for parametric imaging of the brain. *NeuroImage.* 5/1/ 2009;45(4):1183–1189.

27. Dean Fang Y-H, El Fakhri G, Becker JA, Alpert NM. Parametric imaging with Bayesian priors: A validation study with ^{11}C-

Altropane PET. *NeuroImage.* 2012;61(1):131–138.

28. Kamasak M. Effects of spatial regularization on kinetic parameter estimation for dynamic PET. *Biomed Signal Proces.* 2014;9:6–13.

29. Logan J. A review of graphical methods for tracer studies and strategies to reduce bias. *Nucl Med Biol.* 2003;30(8):833–844.

30. Seo S, Kim SJ, Lee DS, Lee JS. Recent advances in parametric neuroreceptor mapping with dynamic PET: Basic concepts and graphical analyses. *Neurosci Bull.* 2014;30(5):733–754.

31. Zhou Y, Ye W, Brašić JR, Wong DF. Multi-graphical analysis of dynamic PET. *NeuroImage.* 2010;49(4):2947–2957.

32. Innis RB, Cunningham VJ, Delforge J, et al. Consensus nomenclature for *in vivo* imaging of reversibly binding radioligands. *J Cereb Blood Flow Metab.* 2007;27(9):1533–1539.

33. Gunn RN, Gunn SR, Cunningham VJ. Positron emission tomography compartmental models. *J Cereb Blood Flow Metab.* 2001;21(6):635–652.

34. Morris ED, Endres CJ, Schmidt KC, Christian BT, Muzic RFJ, Fisher RE. Kinetic modeling in positron emission tomography. In: Wernick MN, Aarsvold JN, eds. *Emission tomography: The fundamentals of PET and SPECT*. San Diego: Academic Press; 2004:499–540.

35. Huang S-C, Barrio JR, Phelps ME. Neuroreceptor assay with positron emission tomography: Equilibrium versus dynamic approaches. *J Cereb Blood Flow Metab.* 1986;6(5):515–521.

36. Lammertsma AA, Hume SP. Simplified reference tissue model for PET receptor studies. *NeuroImage.* 1996;4(3):153–158.

37. Phelps M, Huang S-C, Hoffman E, Selin C, Sokoloff L, Kuhl D. Tomographic measurement of local cerebral glucose metabolic rate in humans with (F-18) 2-fluoro-2-deoxy-$_{D}$-glucose: Validation of method. *Ann Neurol.* 1979;6(5):371–388.

38. Huang S-C, Phelps ME, Hoffman EJ, Sideris K, Selin CJ, Kuhl DE. Noninvasive determination of local cerebral metabolic rate of glucose in man. *Am J Physiol Endocrinol Metab.* 1980;238(1):E69–E82.

39. Ogden RT. Estimation of kinetic parameters in graphical analysis of PET imaging data. *Stat Med.* 2003;22(22):3557–3568.

40. Wu Y-G. Noninvasive quantification of local cerebral metabolic rate of glucose for clinical application using positron emission tomography and ^{18}F-fluoro-2-deoxy-$_{D}$-glucose. *J Cereb Blood Flow Metab.* 2008;28(2):242–250.

41. Zheng X, Wen L, Yu S-J, Huang S-C, Feng DD. A study of non-invasive Patlak quantification for whole-body dynamic FDG-PET studies of mice. *Biomed Signal Proces.* 2012;7(5):438–446.

42. Chen K, Bandy D, Reiman E, et al. Noninvasive quantification of the cerebral metabolic rate for glucose using positron emission tomography, ^{18}F-fluoro-2-deoxyglucose, the Patlak method, and an image-derived input function. *J Cereb Blood Flow Metab.* 1998;18(7):716–723.

43. Kim SJ, Lee JS, Im KC, et al. Kinetic modeling of 3′ -deoxy-3′ -^{18}F-fluorothymidine for quantitative cell proliferation imaging in subcutaneous tumor models in mice. *J Nucl Med.* 2008;49(12):2057–2066.

44. Kim JH, Kim Y-H, Kim YJ, et al. Quantitative positron emission tomography imaging of angiogenesis in rats with forelimb ischemia using ^{68}Ga-NOTA-c(RGDyK). *Angiogenesis.* 2013;16(4):837-846.

45. Feng D, Huang S-C, Wang X. Models for computer simulation studies of input functions for tracer kinetic modeling with positron emission tomography. *Int J Biomed Comput.* 1993;32(2):95-110.

46. Phillips RL, Chen CY, Wong DF, London ED. An improved method to calculate cerebral metabolic rates of glucose using PET. *J Nucl Med.* 1995;36(9):1668-1679.

47. Takikawa S, Dhawan V, Spetsieris P, et al. Noninvasive quantitative fluorodeoxyglucose PET studies with an estimated input function derived from a population-based arterial blood curve. *Radiology.* 1993;188(1):131-136.

48. Cunningham VJ, Hume SP, Price GR, Ahier RG, Cremer JE, Jones A. Compartmental analysis of diprenorphine binding to opiate receptors in the rat in vivo and its comparison with

equilibrium data in vitro. *J Cereb Blood Flow Metab.* 1991;11(1):1–9.

49. Hume SP, Myers R, Bloomfield PM, et al. Quantitation of carbon-11-labeled raclopride in rat striatum using positron emission tomography. *Synapse.* 1992;12(1):47–54.

50. Lammertsma A, Bench C, Hume S, et al. Comparison of methods for analysis of clinical [^{11}C]raclopride studies. *J Cereb Blood Flow Metab.* 1996;16(1):42–52.

51. Watabe H, Carson R, Iida H. The reference tissue model: Three compartments for the reference region. *NeuroImage.* 2000;11(6):S12.

52. Feng D, Wong K-P, Wu C-M, Siu W-C. A technique for extracting physiological parameters and the required input function simultaneously from PET image measurements: Theory and simulation study. *IEEE Trans Inf Technol Biomed.* 1997;1(4):243–254.

53. Watabe H, Channing MA, Riddell C, et al. Noninvasive estimation of the aorta input function for measurement of tumor blood flow

with [^{15}O] water. *IEEE Trans Med Imaging.* 2001;20(3):164–174.

54. Wu H-M, Hoh CK, Choi Y, et al. Factor analysis for extraction of blood time-activity curves in dynamic FDG-PET studies. *J Nucl Med.* 1995;36(9):1714–1722.

55. Lee JS, Lee DS, Ahn JY, et al. Blind separation of cardiac components and extraction of input function from $H_2{}^{15}O$ dynamic myocardial PET using independent component analysis. *J Nucl Med.* 2001;42(6):938–943.

56. Ahn JY, Lee DS, Lee JS, et al. Quantification of regional myocardial blood flow using dynamic $H_2{}^{15}O$ PET and factor analysis. *J Nucl Med.* 2001;42(5):782–787.

57. Naganawa M, Kimura Y, Ishii K, Oda K, Ishiwata K, Matani A. Extraction of a plasma time-activity curve from dynamic brain PET images based on independent component analysis. *IEEE Trans Biomed Eng.* 2005;52(2):201–210.

58. Parker BJ, Feng DD. Graph-based mumford-shah segmentation of dynamic PET with application to input function estimation.

IEEE Trans Nucl Sci. 2005;52(1):79–89.

59. Zanderigo F, Ogden RT, Parsey RV. Reference region approaches in PET: A comparative study on multiple radioligands. *J Cereb Blood Flow Metab.* 2013;33(6):888–897.

60. Logan J, Fowler JS, Volkow ND, Wang G-J, Ding Y-S, Alexoff DL. Distribution volume ratios without blood sampling from graphical analysis of PET data. *J Cereb Blood Flow Metab.* 1996;16(5):834–840.

61. Wong DF, Wagner HN, Dannals RF, et al. Effects of age on dopamine and serotonin receptors measured by positron tomography in the living human brain. *Science.* 1984;226(4681):1393–1396.

62. Beck JV, Arnold KJ. *Parameter estimation in engineering and science*. New York: John Wiley & Sons; 1977.

63. Gjedde A. High- and low-affinity transport of $_{D}$-glucose from blood to brain. *J Neurochem.* 1981;36(4):1463–1471.

64. Patlak CS, Blasberg RG, Fenstermacher JD. Graphical evaluation

of blood-to-brain transfer constants from multiple-time uptake data. *J Cereb Blood Flow Metab.* 1983;3(1):1–7.

65. Patlak CS, Blasberg RG. Graphical evaluation of blood-to-brain transfer constants from multiple-time uptake data. Generalizations. *J Cereb Blood Flow Metab.* 1985;5(4):584–590.

66. Logan J, Fowler JS, Volkow ND, et al. Graphical analysis of reversible radioligand binding from time-activity measurements applied to [*N*-^{11}C-methyl]-(-)-cocaine PET studies in human subjects. *J Cereb Blood Flow Metab.* 1990;10(5):740–747.

67. Yokoi T, Iida H, Itoh H, Kanno I. A new graphic plot analysis for cerebral blood flow and partition coefficient with iodine-123-iodoamphetamine and dynamic SPECT validation studies using oxygen-15-water and PET. *J Nucl Med.* 1993;34(3):498–505.

68. Ito H, Yokoi T, Ikoma Y, et al. A new graphic plot analysis for determination of neuroreceptor binding in positron emission tomography studies. *NeuroImage.* 2010;49(1):578–586.

69. Zhou Y, Ye W, Brašić JR, Crabb AH, Hilton J, Wong DF. A consistent and efficient graphical analysis method to improve

the quantification of reversible tracer binding in radioligand receptor dynamic PET studies. *NeuroImage.* 2009;44(3):661–670.

70. Logan J, Alexoff D, Fowler JS. The use of alternative forms of graphical analysis to balance bias and precision in PET images. *J Cereb Blood Flow Metab.* 2011;31(2):535–546.

71. Schmidt KC, Turkheimer FE. Kinetic modeling in positron emission tomography. *Q J Nucl Med.* 2002;46(1):70–85.

72. Ametamey SM, Treyer V, Streffer J, et al. Human PET studies of metabotropic glutamate receptor subtype 5 with ^{11}C−ABP688. *J Nucl Med.* February 1, 2007 2007;48(2):247−252.

73. Treyer V, Streffer J, Wyss MT, et al. Evaluation of the metabotropic glutamate receptor subtype 5 using PET and ^{11}C−ABP688: Assessment of methods. *J Nucl Med.* July 1, 2007 2007;48(7):1207–1215.

74. Yaqub M, Boellaard R, van Berckel BNM, et al. Quantification of dopamine transporter binding using [^{18}F]FP−β−CIT and positron emission tomography. *J Cereb Blood Flow Metab.*

2007;27(7):1397–1406.

75. Kropholler MA, Boellaard R, Schuitemaker A, et al. Development of a tracer kinetic plasma input model for (*r*)−[^{11}C]PK11195 brain studies. *J Cereb Blood Flow Metab.* 2005;25(7):842–851.

76. Ichise M, Ballinger JR, Golan H, et al. Noninvasive quantification of dopamine D_2 receptors with iodine−123−IBF SPECT. *J Nucl Med.* 1996;37(3):513–520.

77. Carson RE. PET parameter estimation using linear integration methods: Bias and variability considerations. In: Uemura K, Lassen NA, Jones T, Kanno I, eds. *Quantification of brain function: Tracer kinetics and image analysis in brain PET*. Amsterdam: Elsevier Science Publishers; 1993:499–507.

78. Abi−Dargham A, Martinez D, Mawlawi O, et al. Measurement of striatal and extrastriatal dopamine D_1 receptor binding potential with [^{11}C]NNC 112 in humans: Validation and reproducibility. *J Cereb Blood Flow Metab.* 2000;20(2):225–243.

79. Slifstein M, Laruelle M. Effects of statistical noise on graphic analysis of PET neuroreceptor studies. *J Nucl Med.*

2000;41(12):2083–2088.

80. Kimura Y, Naganawa M, Shidahara M, Ikoma Y, Watabe H. PET kinetic analysis—pitfalls and a solution for the Logan plot. *Ann Nucl Med.* 2007;21(1):1–8.

81. Ikoma Y, Takano A, Varrone A, Halldin C. Graphic plot analysis for estimating binding potential of translocator protein (TSPO) in positron emission tomography studies with [^{18}F]FEDAA1106. *NeuroImage.* 2013;69:78–86.

82. Brooks D, Salmon E, Mathias C, et al. The relationship between locomotor disability, autonomic dysfunction, and the integrity of the striatal dopaminergic system in patients with multiple system atrophy, pure autonomic failure, and parkinson's disease, studied with PET. *Brain.* 1990;113(5):1539–1552.

83. Howes OD, Montgomery AJ, Asselin M, Murray RM, Grasby PM, McGUIRE PK. Molecular imaging studies of the striatal dopaminergic system in psychosis and predictions for the prodromal phase of psychosis. *Br J Psychiatry.* 2007;191(51):s13–s18.

84. Howes OD, Montgomery AJ, Asselin M-C, et al. Elevated striatal dopamine function linked to prodromal signs of schizophrenia. *Arch Gen Psychiatry.* 2009;66(1):13–20.

85. Kumakura Y, Cumming P. PET studies of cerebral levodopa metabolism: A review of clinical findings and modeling approaches. *Neuroscientist.* 2009;15(6):635–650.

86. Chaly T, Dhawan V, Kazumata K, et al. Radiosynthesis of [^{18}F] n-3-fluoropropyl-2-β-carbomethoxy-3-β-(4-iodophenyl) nortropane and the first human study with positron emission tomography. *Nucl Med Biol.*23(8):999–1004.

87. Ichise M, Liow J-S, Lu J-Q, et al. Linearized reference tissue parametric imaging methods: Application to [^{11}C]DASB positron emission tomography studies of the serotonin transporter in human brain. *J Cereb Blood Flow Metab.* 2003;23(9):1096–1112.

88. Seo S, Kim SJ, Kim YK, et al. Comparative assessment of parametric neuroreceptor mapping approaches based on the simplified reference tissue model using [^{11}C]ABP688 PET. *J Cereb Blood Flow Metab.* 12//print 2015;35(12):2098–2108.

89. Wu Y, Carson RE. Noise reduction in the simplified reference tissue model for neuroreceptor functional imaging. *J Cereb Blood Flow Metab.* 12//print 2002;22(12):1440–1452.

90. Lundkvist C, Halldin C, Ginovart N, Swahn CG, Farde L. [^{18}F]β-CIT-FP is superior to [^{11}C]β-CIT-FP for quantification of the dopamine transporter. *Nucl Med and Biol.* 1997;24:621-627.

91. Eo J, Lee H-Y, Lee J, Kim Y, Jeon B-S, Lee D. Automated analysis of ^{123}I-beta-CIT SPECT images with statistical probabilistic anatomical mapping. *Nucl Med Mol Imaging.* 2014/03/01 2014;48(1):47–54.

92. Jin S, Oh M, Oh S, et al. Differential diagnosis of parkinsonism using dual-phase F-18 FP-CIT PET imaging. *Nucl Med Mol Imaging.* 2013/03/01 2013;47(1):44–51.

93. Park E, Hwang Y, Lee C-N, et al. Differential diagnosis of patients with inconclusive parkinsonian features using [^{18}F]FP-CIT PET/CT. *Nucl Med Mol Imaging.* 2014/06/01 2014;48(2):106–113.

94. Wang J, Zuo C-T, Jiang Y-P, et al. ^{18}F-FP-CIT PET imaging and spm analysis of dopamine transporters in Parkinson's disease in various hoehn & yahr stages. *J Neurol.* 2007;254(2):185-190.

95. Ma Y, Dhawan V, Mentis M, Chaly T, Spetsieris PG, Eidelberg D. Parametric mapping of [^{18}F]FPCIT binding in early stage parkinson's disease: A PET study. *Synapse.* 2002;45:125-133.

96. Jeong E, Oh S, Pahk K, et al. Feasibility of PET template-based analysis on F-18 FP-CIT PET in patients with de novo Parkinson's disease. *Nucl Med Mol Imaging.* 2013;47(2):73–80.

97. Kim Y-i, Im H-J, Paeng J, et al. Validation of simple quantification methods for ^{18}F-FP-CIT PET using automatic delineation of volumes of interest based on statistical probabilistic anatomical mapping and isocontour margin setting. *Nucl Med Mol Imaging.* 2012;46(4):254–260.

98. Seo M, Oh M, Cho M, Chung S, Lee C, Kim J. The effect of SSRIs on the binding of ^{18}F-FP-CIT in parkinson patients: A retrospective case control study. *Nucl Med Mol Imaging.* 2014/12/01 2014;48(4):287–294.

99. Lee J-Y, Seo S, Lee JS, Kim H-J, Kim YK, Jeon BS. Putaminal serotonergic innervation: Monitoring dyskinesia risk in parkinson disease *Neurology.* 2015;85(10):853–860.

100. Wong K-P, Kepe V, Dahlbom M, et al. Comparative evaluation of Logan and relative-equilibrium graphical methods for parametric imaging of dynamic [^{18}F]fddnp PET determinations. *NeuroImage.* 2012;60(1):241–251.

101. Wentao Z, Ning G, Bing B, Conti PS, Leahy RM, Quanzheng L. Direct estimation from list-mode data for reversible tracers using graphical modeling. *Biomedical Imaging (ISBI), 2015 IEEE 12th International Symposium on*; 2015:1204–1207.

102. Wentao Z, Quanzheng L, Bing B, Conti PS, Leahy RM. Patlak image estimation from dual time-point list-mode PET data. *IEEE Trans Med Imaging.* 2014;33(4):913–924.

103. Yaqub M, Boellaard R, Kropholler MA, Lammertsma AA. Optimisation algorithms and weighting factors for analysis of dynamic PET studies. *Phys Med Biol.* 2006;51(17):4217–4232.

초 록

동적 양전자단층촬영(positron emission tomography, PET) 기반의 추적자 동역학 모델링(tracer kinetic modeling)은, 뇌신경수용체 결합(neuroreceptor binding)에 대한 정량적 파라미터의 영상, 즉, 파라메트릭 영상(parametric image)의 생성을 가능하게 함으로써, 뇌질환에서의 뇌신경수용체의 특징적 분포 패턴 또는 기능 장애를 연구하는데 널리 쓰여져 왔다. 도표분석법(graphical analysis, GA)은 동역학 모델링 이론에 기반한 대표적인 파라메트릭 영상화(parametric imaging) 기술로서, 더 복잡한 구획 모델(compartment model)을 선형화 및 단순화하여 얻어진 단순선형회귀분석모델(simple linear regression model)에 기반하고 있다. 이러한 단순선형 모델은 바람직한 파라메트릭 영상 생성을 가능하게 하지만, 다양한 GA 방법들의 각 모델들은 각 방법들마다 고유한 몇 가지 가정에 기반하고 있다. 느린 동역학을 보이는 추적자를 위한 파라메트릭 영상화의 경우에는, 이러한 가정들은 서로 동시에 만족하기가 어려우며, 이로 인해 파라미터 추정에 오류를 야기하게 된다. 두 가지 도표분석법을 결합한 이중도표분석법(bi-graphical analysis)을 이용하면, 동적 PET 데이터를 통해 얻어진 시공간 정보 및 개별 도표분석법의 장점들을 충분히 활용함으로써, 도표분석법에 내재된 이러한 문제를 개선할 수 있다.

본 연구는 가역적 뇌신경수용체 결합의 파라메트릭 영상화를 위한 이중도표분석법을 다룬다. 이를 위하여, 첫 번째로는, 동적 뇌신경수용체 PET을 이용한 도표분석법 기반의 파라메트릭 영상화 기술에서의 최신 지견을 소개한다. 주요 구획모델 및 관심 파라미터들(parameters of interest) 등,

추적자 동역학 모델링에서의 기초 개념들을 알아보고, 가역(reversible) 및 비가역(irreversible) 방사성리간드(radioligand)를 위한 GA 방법들의 기술적 세부사항들에 대해서도, 동맥혈장입력함수(arterial plasma input function)를 이용하는 모델과 참고영역입력함수(reference region input function)에 기반한 모델들로 나누어 살펴본다. 각 GA 방법들의 기저 가정들과 통계적 특성들도 파라메트릭 영상화의 관점에서 기술한다.

다음으로, 느린 결합 속도로 인해 PET 촬영 동안에는 상대적 평형(relative equilibrium, RE) 상태에 도달하기 어려운 가역 방사성리간드 결합의 정량화를 위한, 새로운 참고영역기반(또는 비침습적, noninvasive) 이중도표분석법을 제안한다. 제안된 방법은, 기존의 비침습적 Logan plot 방법을 간접적으로 구현할 수 있는 방법으로, 다른 두 가지 GA 방법들로 추정한 파라미터들과 참고영역의 겉보기 조직-혈장간 유출속도상수(apparent tissue-to-plasma efflux rate constant for the reference region, k_2') 간의 산술연산을 이용하여 관심 파라미터를 계산한다. 본 연구에서는, 다양한 잡음 수준(noise levels)과 k_2' 값들에 대한 모의실험(simulation)을 통해, 제안된 방법의 타당성을 검증하고 그 통계적 특성을 조사하였다. 또한 인간 뇌의 [^{18}F]FP-CIT PET 연구에의 적용가능성도 평가하였다.

실험 결과에 따르면, 낮은 잡음 수준에서는, 제안된 방법이 Logan plot 방법과 유사한 관심 파라미터 추정 결과를 보이며, 동시에 그 결과값들은 상대적 비평형에 기인한 과소추정(non-RE-induced underestimation) 문제를 개선하는데, 그 정도는 k_2' 값에 의해 결정이 된다. 또한, 높은 잡음 수준에서는, 제안된 방법이 Logan plot 방법에서의 잡음으로 인한 편향(noise-induced bias) 문제를 개선할 수 있고, 추정 결과값의 변동성

(variability)도 Logan plot 방법에 비해서 k_2'값의 영향을 덜 받는 것을 확인하였다. 종합하여 볼 때, 결론적으로, 제안된 방법은, k_2'의 사전추정값이 주어지면 동맥혈추출과 관련된 문제를 피할 수 있는 비침습적 방법으로, 느린 동역학으로 인해 PET 촬영 동안에는 상대적 비평형(non-RE) 상태에 머무를 수 밖에 없는 가역 추적자를 이용한 연구에서, 우수한 품질의 파라메트릭 영상을 생성하는데 유용한 방법이 될 것으로 기대한다.

주요어 : 도표분석법, 참고영역, 파라메트릭 영상, 뇌신경수용체 영상화, 추적자 동역학 모델링, 동적 양전자단층촬영

학 번 : 2010-30768